

Physics-constrained Gaussian Processes for Predicting Shockwave Hugoniot Curves

George D. Pasparakis^{a,*}, Himanshu Sharma^a, Rushik Desai^b, Chunyu Li^b, Alejandro Strachan^b, Lori Graham-Brady^a, Michael D. Shields^a

^a*Department of Civil and Systems Engineering, Johns Hopkins University, Baltimore, Maryland, USA*

^b*School of Materials Engineering, Purdue University, West Lafayette, Indiana, USA*

Abstract

A physics-constrained Gaussian Process regression framework is developed for predicting shocked material states along the Hugoniot curve using data from a small number of shockwave simulations. The proposed Gaussian process employs a probabilistic Taylor series expansion in conjunction with the Rankine–Hugoniot jump conditions between the various shocked material states to construct a thermodynamically consistent covariance function. This leads to the formulation of an optimization problem over a small number of interpretable hyperparameters and enables the identification of regime transitions, from a leading elastic wave to trailing plastic and phase transformation waves. This work is motivated by the need to investigate shock-driven material response for materials discovery and for offering mechanistic insights in regimes where experimental characterizations and simulations are costly. The proposed methodology relies on large-scale molecular dynamics which are an accurate but expensive computational alternative to experiments. Under these constraints, the proposed methodology establishes Hugoniot curves from a limited number of molecular dynamics simulations. We consider silicon carbide as a representative material and atomic-level simulations are performed using a reverse ballistic approach together with appropriate interatomic potentials. The framework reproduces the Hugoniot curve with satisfactory accuracy while also quantifying the uncertainty in the predictions using the Gaussian Process posterior.

1. Introduction

Large-amplitude wave propagation in solids induced by a high-velocity impact is governed by the constitutive behavior of materials. The response of the material to the dynamical insult encompasses a broad range of physical phenomena, including elasticity, thermodynamics, phase transformations, plasticity, and distinct failure mechanisms. Experimental investigation and analysis of shockwave propagation provide a powerful means of understanding this material response under extreme dynamic conditions and can offer critical insights into the underlying physics. However, experimental characterization of shock response poses numerous challenges. A considerable level of complexity arises due to the sensitivity in loading

*Corresponding author

parameters such as sample confinement, impact angle, sample alignment, and crystal orientation relative to the shock propagation, resulting in a large number of experimental scenarios [1]. This is coupled with extremely fast time scales, in which the material transitions from the unloaded to the shocked state in a matter of picoseconds. This transition manifests itself as a discontinuity of near-atomic thickness between the two states, which is very difficult to measure accurately. Further complicating the process, the resulting extreme pressures and temperatures result in plastic deformation, phase transitions, and chemical reactions.

To complement experiments, the research community developed advanced computational models. Molecular dynamics (MD) is a particularly powerful method that can provide insights into the underlying physics of the shock response [2]. Early work on metals revealed the atomistic mechanisms behind plastic deformation [3], phase transitions [4] and dynamic failure [5]. Recently, larger-scale simulations and more broadly applicable interatomic potentials have enabled the simulation of more complex materials and physico-chemical processes [6–8]. Despite demonstrating good agreement with experimental data, see e.g. [9], large-scale MD simulations can be computationally demanding. Shock simulations typically scale quadratically with system length as increasing the length of the simulation requires increasing the simulation time. A typical 200 M atom shock simulation requires \sim 7000 CPU hours for 40000 steps with 1fs timestep using AMD Epyc 7763 “Milan” CPUs @ 2.2GHz.

To mitigate the computational burden, machine learning methods can be employed to generate shock response data and, more broadly, to predict material behavior. For example, neural network-based approaches have shown promise in developing interatomic potentials [10], generating samples from equilibrium distributions [11], predicting full-field material responses [12], and mapping microstructure to thermal response under shock loading [13]. However, neural network-based approaches require a large amount of training data, which is often difficult or infeasible to obtain. Furthermore, these approaches are not accompanied by uncertainty quantification (UQ) capabilities. Accounting for this limitation, in this study a Gaussian process regression (GPR) framework is developed as a data-efficient, non-parametric Bayesian alternative method that not only performs well with limited training samples but also naturally provides predictive uncertainty estimates [14]. The reliance on training data can be further reduced by incorporating physical constraints into the GP framework, which also ensures realistic predictions. Recent studies [15, 16] have introduced physics-constrained GPR frameworks for data-driven materials modeling and demonstrated their effectiveness under limited data conditions. Motivated by these developments, a physics-constrained GPR framework is proposed for predicting shocked material states along the Hugoniot. This approach applies to a broad class of materials by adhering to fundamental conservation laws across the shock front. Specifically, the framework enforces the Rankine–Hugoniot conditions as physical constraints by deriving a physics-based covariance function, constructed using a Taylor series expansion, that inherently satisfies these conditions. The proposed method is capable of modeling the transition from purely elastic shock response to elastic response with a trailing plastic wave, and ultimately into the overdriven regime. The model relies on a small number of interpretable parameters and is analytically shown to be consistent with the laws of thermodynamics.

The model is applied to Silicon Carbide (SiC) as a representative material. SiC is a highly versatile engineering material that possesses exceptional physical properties, such as high thermal conductivity, stiffness, and hardness along with low density. It is shown that

the proposed method can model SiC Hugoniot behavior in a computationally inexpensive manner using limited MD simulation data while also quantifying the uncertainty in the estimated state.

2. Background

Shock-compression occurs when a material is subjected to an abrupt, high-speed impact or loading event, whose duration is considerably shorter than the characteristic time for the material to respond through inertial motion. For sufficiently high impact velocities, a structured wave with very short rise time (sub-picoseconds within single crystals) forms such that the thickness of the wave front can be ignored or cannot be measured experimentally. This leads to a jump in the principal mechanical and thermodynamic variables such as pressure, strain, velocity, and temperature. A schematic representation of shock wave loading is shown in Fig. 1, where a projectile impacts the material at piston velocity u_p . The shock wave travels through the medium with velocity u_s , which is hypersonic relative to the unperturbed material, while the material behind the shock front moves at the particle velocity v_z relative to a stationary frame of reference (shown here as the initial boundary of the undeformed material).

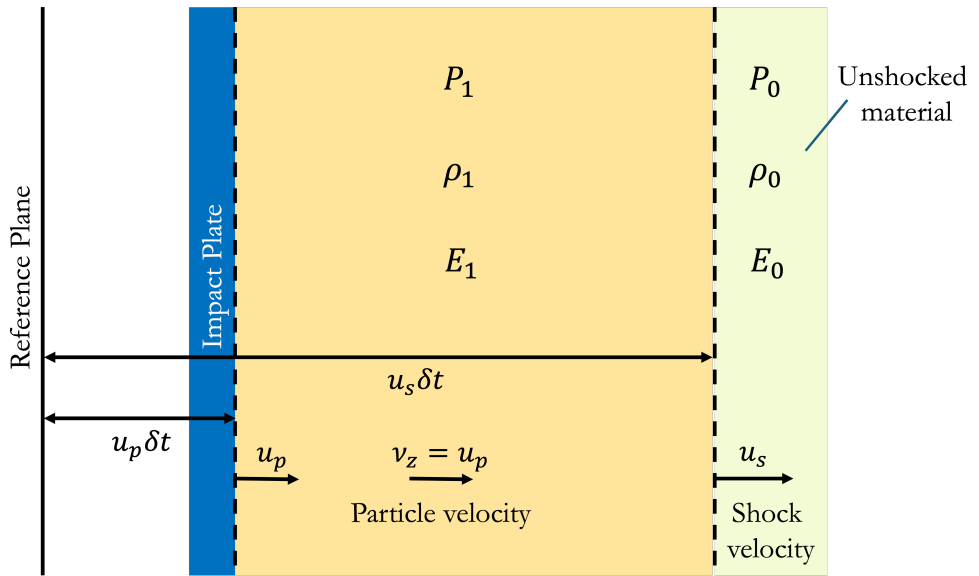


Figure 1: Schematic representation of shock wave propagation in a material element.

In a shock wave, gradients of the thermomechanical parameters in the unperturbed regions of the material are negligible compared to gradients at the shock front. This gives rise to a jump at the shock front. For steady-state shocks, applying conservation of mass, momentum, and energy across the jump gives relationships between the material state ahead of the shock (the “initial state”) and the state behind the shock front (the “final state”). These are commonly referred to as the Rankine-Hugoniot jump conditions, in which the shock wave is characterized by a jump in pressure, density, and temperature across the wave front. For a single wave propagating in an unperturbed material, the corresponding Rankine-Hugoniot

equations are given by [17]

$$P = \rho_0 u_s u_p + P_0 \quad (1)$$

$$\rho = \frac{\rho_0 u_s}{u_s - u_p} \quad (2)$$

$$E = E_0 + \frac{1}{2} (\rho_0^{-1} - \rho^{-1}) (P + P_0) \quad (3)$$

such that pressure P , density ρ , and internal energy E in the shocked material can be calculated from the initial unperturbed states P_0 , ρ_0 , E_0 together with the shock velocity u_s and the particle velocity u_p . From a known ambient initial state, these three coupled equations can be solved for the shocked state by measuring u_s and u_p experimentally or from simulations.

A complete description of the thermodynamic state (i.e., closure of the system of equations) is achieved by introducing a fourth relation, typically in the form of an equation of state (EOS) model that relates the thermodynamic variables P, V (or ρ), T, E under shock conditions. Depending on the initial conditions, these relations define a set of thermodynamically accessible states in the $(P - V - T)$ space under shock conditions. Importantly, the temperature (T) in the shocked state cannot be derived directly from the Hugoniot equations without assuming an equation of state or measured experimentally in a straightforward manner, but can be obtained from MD simulations or estimated as [2]:

$$E - E_0 = \int_{T_0}^T C_v(T') dT' \quad (4)$$

where $C_v(T)$ is the specific heat (which is assumed to be independent of pressure).

Under shock conditions, solids exhibit a threshold value of elastic deformation after which plastic deformation is initiated. When the imparted particle velocity induces stresses that result in plastic deformation, the material is said to reach its Hugoniot Elastic Limit (HEL). For shock scenarios below the HEL, a distinct elastic wave forms and propagates with velocity u_s as illustrated in Figure 1 and shown in the left-most “Elastic” region in Figure 2 relating u_s and u_p for SiC from MD shock simulations. For imparted particle velocities above the HEL, a two-wave structure is often observed with an elastic leading wave (denoted by blue x’s in the “Elastic-Plastic” regime in Figure 2) having shock velocity u_{s1} followed by a trailing plastic wave having shock velocity u_{s2} (denoted by red x’s in Figure 2). Above a certain particle velocity ($u_p > 2.5$ km/s), the trailing plastic wave and the elastic wave merge to form a single plastic leading wave, this happens for our example at a particle velocity above 2 km/s. Driving to higher shock velocities can result in additional processes. In the SiC case shown, a trailing phase transformation wave forms (denoted by green x’s in Figure 2), which again increases in velocity with higher particle velocity. Finally, in the “overdriven” state, a single phase transition leading wave forms with increasing shock velocity.

The objective of this work is to derive and generate a machine learning model capable of predicting shock velocity, pressure, and other thermodynamic variables for a given shock scenario (i.e. a prescribed u_p) that is constrained by shock physics (e.g., Rankine-Hugoniot equations in Eqs. (1)–(3)) and trainable from a limited number of MD simulations such as the data shown in Figure 2. Note that direct application of the Rankine-Hugoniot equations in the form of Eqs. (1)–(3) cannot describe the material behavior in the dual-wave regime.

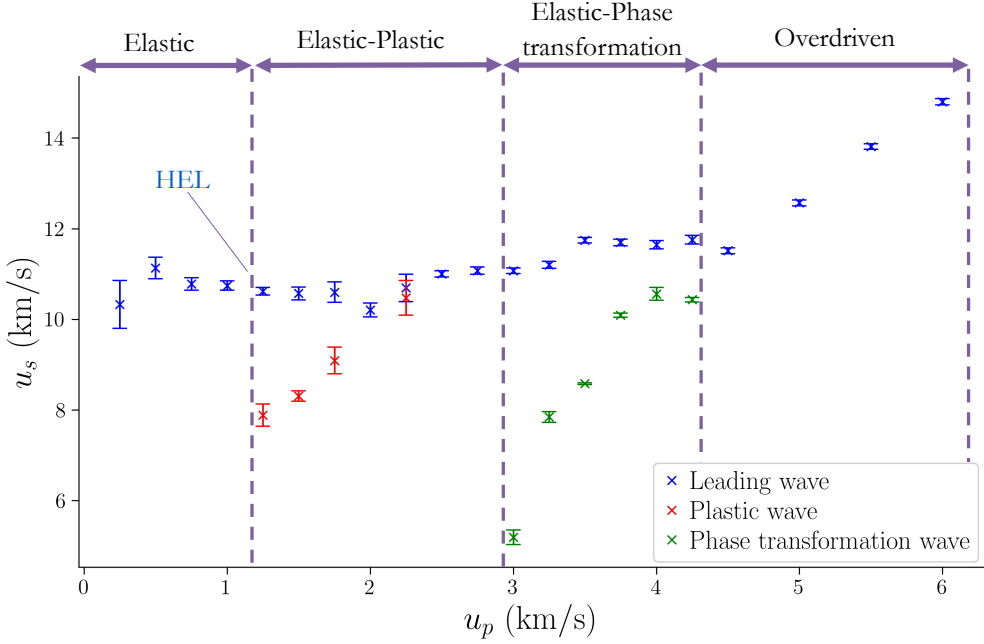


Figure 2: Shock velocity (u_s) vs. particle velocity (u_p) for single crystal SiC in the $[0, 0, 1]$ orientation. Each ‘x’ denotes a mean value \pm one standard deviation from MD simulations. Four regions are denoted. In the ‘Elastic’ regime, a single elastic wave forms as shown by the blue x’s. In the ‘Elastic-Plastic’ regime, a leading elastic wave forms (blue x’s) and is trailed by a plastic wave (red x’s) whose shock velocity increases with increasing particle velocity until the two waves merge. In the ‘Plastic-Phase Transformation’ regime, a leading plastic wave forms (blue x’s) with a trailing phase transformation wave (green x’s). In the ‘Overdriven’ regime, a single phase transformation leading wave forms whose shock velocity increases with increasing particle velocity.

A generalized formulation that accounts for these effects is presented next in Section 2.1. We then introduce the MD shock simulations and the process for extracting relevant data from them. Concluding this section, we present the basics of Gaussian process regression that will be needed for the formulation.

2.1. Generalized Rankine-Hugoniot conditions for multiple shockwaves

To account for the presence of the dual-wave structure, we present here a generalized formulation of the Rankine-Hugoniot conditions. This approach will enable the construction of a unified physics-constrained GP model in Section 4, without requiring a distinct model for each wave. The generalized formulation is based on the assumption that the trailing shock wave propagates through a material that is already in motion. The two-wave structure is then characterized by a leading wave and a trailing plastic or phase-transformation wave.

Because the particle velocities for the two waves are distinct and not necessarily equal to the imparted particle (piston) velocity u_p , we introduce the generalized particle velocity ν_{z_i} corresponding to the i^{th} wave. In the single-wave case, we have $\nu_{z_0} = 0$ as the particle velocity in the unshocked material ahead of the shockwave and $\nu_{z_1} = u_p$ trailing the wave. In the dual-wave case, we have $\nu_{z_0} = 0$ again as the particle velocity in the unshocked material, ν_{z_1} as the particle velocity in the wake of the leading wave measured from MD simulations, and $\nu_{z_2} = u_p$. Each wave is therefore characterized by the particle velocity ν_{z_i}

and corresponding shock velocity u_{s_i} , where again ν_{z_1}, u_{s_1} correspond to the leading wave and ν_{z_2}, u_{s_2} are associated with the trailing plastic or phase transformation wave. Furthermore, each region of material is characterized by its thermodynamic state variables P_i, ρ_i, E_i, T_i , where again the subscript i is used to denote material trailing the i th wave. This is shown schematically in Fig. 3.

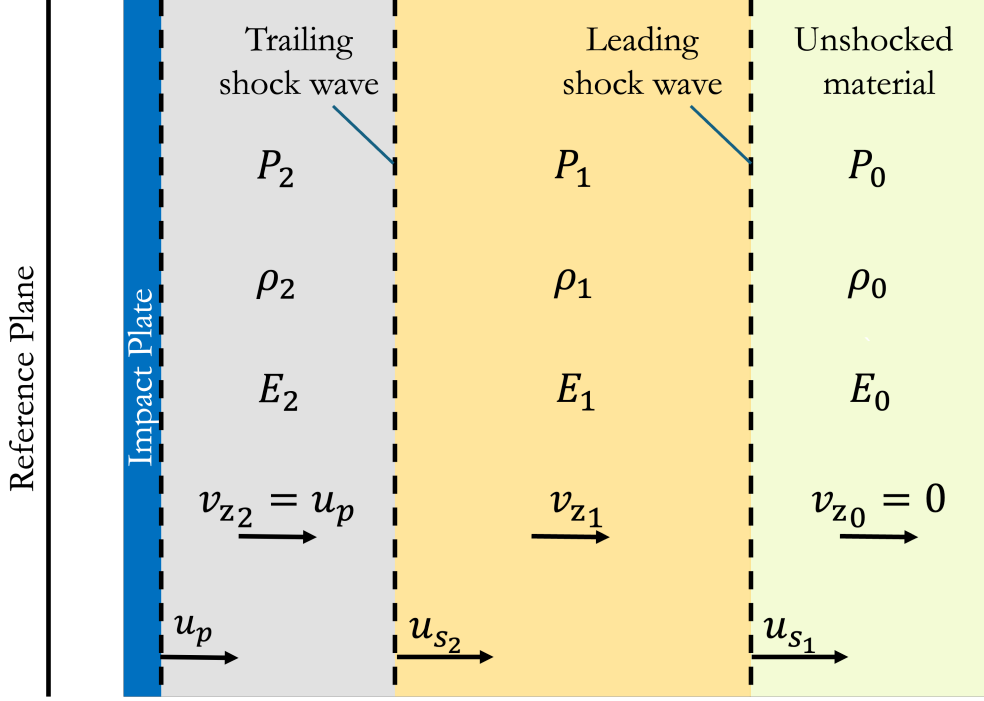


Figure 3: Schematic of shock wave propagation resulting in a two-wave structure.

Applying conservation of mass across the i^{th} propagating wave front, we obtain

$$\rho_{i-1}(u_{s_i} - \nu_{z_{i-1}}) = \rho_i(u_{s_i} - \nu_{z_i}) \quad (5)$$

and rearranging with respect to ρ_i yields

$$\rho_i = \rho_{i-1} \frac{u_{s_i} - \nu_{z_{i-1}}}{u_{s_i} - \nu_{z_i}} \quad (6)$$

Clearly, for the case of a single elastic wave where $\nu_{z_0} = 0$ and $\nu_{z_1} = u_p$, Eq. (6) simplifies to

$$\rho_1 = \rho_0 \frac{u_{s_1}}{u_{s_1} - u_p} = \rho_0 \frac{u_{s_1}}{u_{s_1} - u_p} \quad (7)$$

which is identical to Eq. (2). Likewise, applying conservation of momentum and energy to each shockwave yields the remaining generalized Hugoniot jump conditions given by

$$P_i = \rho_{i-1}(u_{s_i} - \nu_{z_{i-1}})(\nu_{z_i} - \nu_{z_{i-1}}) + P_{i-1} \quad (8)$$

$$E_i = E_{i-1} + \frac{1}{2}(P_i + P_{i-1}) \left(\frac{1}{\rho_{i-1}} - \frac{1}{\rho_i} \right) \quad (9)$$

Taken together, Eqs. (6), (8), and (9) comprise the generalized Rankine-Hugoniot equations for multi-shock wave states. Note these generalized conditions may be applied to materials with any number of parallel shock fronts. For example, one might conceivably apply them to conditions where multiple successive shocks are imparted on the material. In this work, we will only consider the case where a single shock is imparted on the material with up to two shock fronts forming.

3. Molecular Dynamics Simulations for Shockwave Propagation in SiC

SiC has multiple polytypes, and we chose 3C-SiC (also called β -SiC) due to its rich shock response. It has a cubic zinc-blende structure with a lattice constant of 4.354 Å. Each silicon atom is tetrahedrally bonded to four carbon atoms, and vice versa, forming a strong covalent network. MD shock simulations were conducted using the open source code LAMMPS[18] from Sandia National Laboratories with an interatomic potential developed by Vashishta et al. [19], which has been very successful in capturing basic physical and mechanical properties of SiC.

The shock simulations used the reverse ballistic approach, where a pre-equilibrated target sample is launched into a fixed piston with a velocity $-u_p$. The impact launches a shock wave in the target in the direction opposite to u_p . The temporal evolution of the system is described via adiabatic MD (NVE ensemble) with a timestep of 1 fs. The (001) plane was chosen as the impact plane, thus the shock wave propagates in the [001] direction. The target is formed by replicating the 8-atom unit cell $60 \times 60 \times 1020$ times along [001], [010], and [001], respectively, resulting in cross-sectional dimensions of 25nm \times 25nm and a length of \sim 450 nm. The fixed piston has the same cross section as the target and a thickness of 2 nm. The initial gap between the piston and target is 2 nm. The total system has 28,587,552 atoms and periodic boundary conditions are imposed in the transverse directions. A schematic setup is shown in Figure 4(a), together with snapshots of shocks of different strengths.

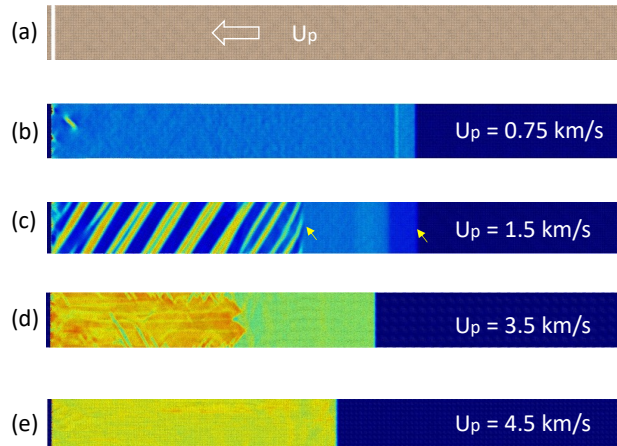


Figure 4: Shock wave simulations in MD: (a) Schematic setup; (b) Elastic wave propagation from $u_p = 0.75$ km/s. (c) Dual elastic-plastic wave formation from $u_p = 1.5$ km/s. (d) Dual plastic-phase transformation wave formation from $u_p = 3.5$ km/s. (e) Overdriven shock propagation. In all figures, colors show atomic shear strains.

3.0.1. Temperature, Density, and Stress Profiles

We studied a series of particle velocities, ranging from 0.25 km/s to 6.0 km/s in increments of 0.25 km/s. The simulations were stopped at 36 ps, before the shock wave reached the free surface of the target. For weak shocks, we observe a purely elastic wave, but increasing the shock strength beyond the HEL results in plastic deformation and a phase transition. The snapshots colored by shear strain shown in Figure 4 clearly display the wave fronts.

The shock front is marked by sharp changes in local properties, including density, velocity, temperature, and stress. To analyze the MD simulations and extract consistent and reproducible information to train the GP model, we developed and implemented an automatic workflow consisting of several steps described here and in the following sub-section. The first step is to divide the simulation domain into thin bins and average properties or parameters over the bins. We performed a one-dimensional binning in the shock direction with a bin size of 2 nm. The temperature, density, and stress profiles are then determined as follows.

The temperature per bin is calculated using the relationship between kinetic energy and temperature, i.e.,

$$\sum_i m_i v_i^2 = k_B T N_{dof} \quad (10)$$

where the sum runs over the atoms i within the bin, m_i and v_i are, respectively, the atomic mass and velocity referenced to the center of mass velocity of the bin, k_B is the Boltzmann constant, and $N_{dof} = 3N - 6$ is the total number of degrees of freedom for the N atoms in a bin. We averaged the per-bin temperature over 1 ps and output the temperature data for each bin accompanying with the spatial bin center. Similarly, we can obtain stress (or pressure) profiles. The atomic stress tensor ($\sigma_{\alpha\beta}$) can be calculated by using the following stress definition[20, 21]:

$$\sigma_{\alpha\beta}^i = -\frac{1}{\Omega^i} [m^i v_\alpha^i v_\beta^i + \frac{1}{2} \sum_{j \neq i} (r_\alpha^{ij} F_\beta^{ij}) + \frac{1}{3} \sum_{j,k} (r_\alpha^{ij} F_\beta^{ijk})] \quad (11)$$

where Ω , m , and v are the atomic volume, mass, and velocity subtracted by the bin center of mass motion, respectively. The first term is the kinetic energy contribution. The second term is the pairwise energy contribution, and the third term is the contribution from three-body interactions. r and F represent the atom position and the corresponding force on the central atom and those involved in the specific interaction. The stresses were averaged over the number of atoms per bin and further averaged over a period of 1 ps and then output for each bin together with the spatial bin center. The density is in units of g/cm³ and is calculated as the total mass of atoms in a bin divided by the volume of the bin.

Figure 5 shows temperature, density, stress, and velocity profiles for selected particle velocities: $u_p = 0.75$ km/s, 1.5 km/s, 3.5 km/s, and 4.5 km/s. The wave propagation can be easily identified from the sharp change in properties. As detailed below, the shock velocity u_s is obtained from the shock front position at various times. For $u_p = 0.75$ km/s in Figure 5(a1), (b1), and (c1), a single elastic shock front is observed having relatively constant density and stress behind the wave front. Increasing the shock strength to 1.5 km/s in Figure 5(a2), (b2), and (c2) results in two wave fronts. The trailing plastic wave has higher density, temperature, and stress than the leading elastic wave. The shear strain snapshot in Figure 4(c) clearly shows the corresponding plastic strain pattern. For $u_p = 3.5$

km/s, we observe two waves from the temperature and density profiles in Figures 5(a3), (b3). Interestingly, the second wave is barely noticeable in the stress profile in Figure 5(c3). This is because energy is mostly converted to internal heat without increasing pressure when SiC undergoes a phase transformation, as previously reported [22, 23]. For particle velocity $u_p = 4.5$ km/s, there is clearly only one phase transformation wave from each of the profiles.

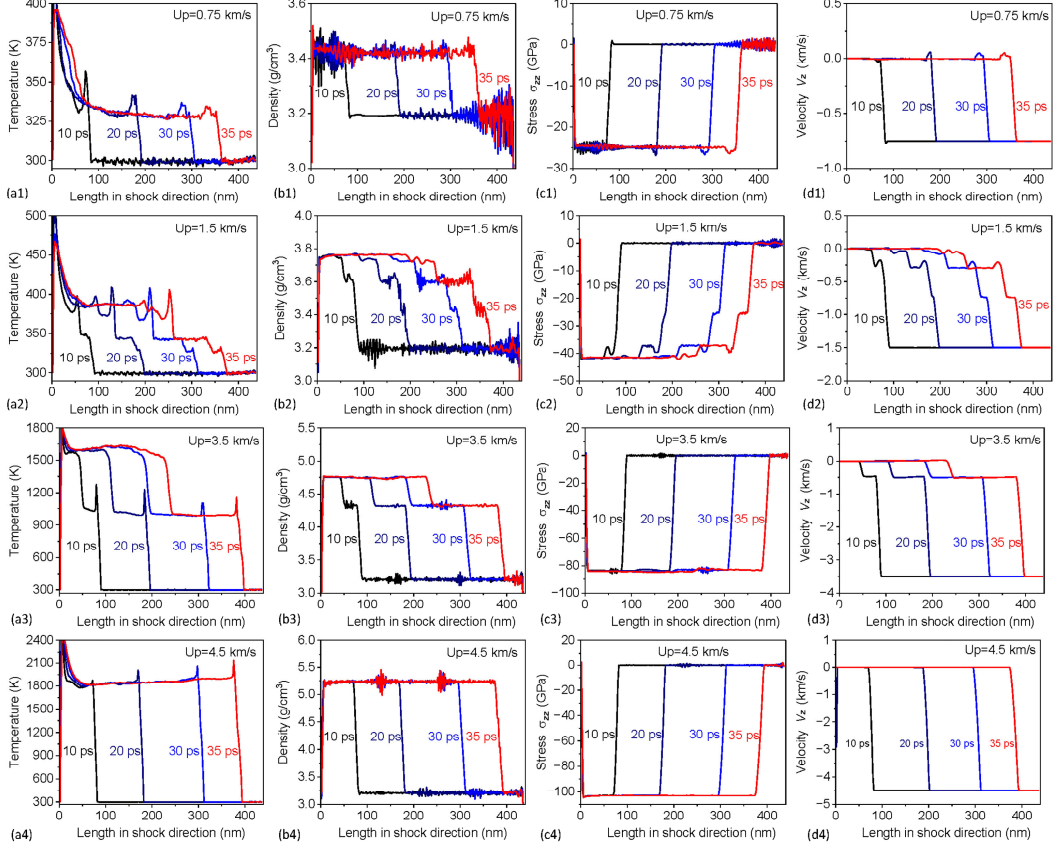


Figure 5: Profiles of (a) temperature, (b) mass density, (c) total stress σ_{zz} along shock direction (z : [001]), and (d) particle velocity from MD shock simulations at (1) $u_p = 0.75$ km/s, (2) $u_p = 1.5$ km/s, (3) $u_p = 3.5$ km/s, and (4) $u_p = 4.5$ km/s.

3.0.2. Shock Property Extraction

Extracting meaningful data from shock simulations, including the identification of wave fronts and the calculation of wave speeds and averaged properties of the shock material, is typically done by hand. This results in tedious manual work and poor reproducibility. To address these issues, we automated and scripted not only the data extraction from the MD simulations but also their subsequent analysis. Property profiles, such as those shown in Figure 5, are utilized to calculate shock speeds and the materials properties on both sides of the shockwave. Our approach involves identifying the shock front(s) and then using this information at various times to calculate the quantities of interest. Importantly, we use the jump conditions to verify the calculations. The Hugoniot jump conditions apply to steadily propagating waves with properties as shown in Figure 3.

The automated workflow illustrated in Figure 6 takes the property profiles as inputs and returns the shock speed(s) and the shock state properties for a given u_p . To identify the shock front(s) from the profiles, we first identify regions where properties are constant by performing a cluster analysis of the property values; these clusters denote the various states of the system (e.g., unshocked, elastically deformed, plastically deformed). While multiple

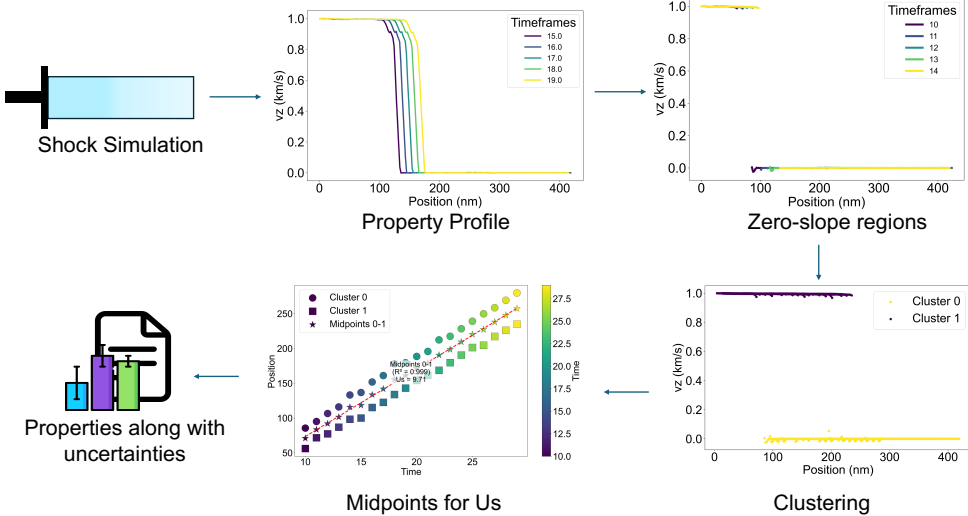


Figure 6: The workflow we utilize to get shock speeds from a property profile obtained from LAMMPS simulation. Then we cluster the zero-sloped regions together. Using the cluster we get the quasi-equilibrium state properties. Midpoints between different cluster boundaries are computed and shock speed is obtained as shown. At the end we save each property along with the standard deviation in the cluster averaging.

properties can be used to identify shock fronts, not all property profiles are equally noise-proof for automated clustering. We studied various properties with different clustering algorithms and parameters at different piston velocities to determine which property would be most suitable for clustering. We find that particle velocity and density are the best properties to identify the number of clusters and hence the wavefronts. We used the hierarchical density-based spatial clustering of applications with noise (HDBSCAN)[24] algorithm due to its known applications in noise-containing data implemented within the scikit-learn library[25].

Using the resulting clusters at a given time, we define shock fronts as the midpoint between the start and end of subsequent regions. The change in position of these midpoints with time is the shock speed U_s , we obtain average velocities by fitting the position vs time data with linear functions. The R^2 obtained from the linear fitting of the midpoints was used to determine the optimal property for clustering. To validate the automatic data analysis and confirm the steady nature of the shocks, we calculate u_s from the averaged pre- and post-shock properties using the jump conditions and compare it with the results of the linear fit. If the difference is larger than the propagated error, the process stops and gives a warning. Figure 7 shows that, apart from a few points, the data match the jump conditions well. Higher errors in momentum conservation arise from error propagation in the stresses, which have the highest deviations.

The workflow generates quasi-equilibrium state values for properties: stress, velocity, density, temperature, and energy, including their standard deviations and shock speeds. The

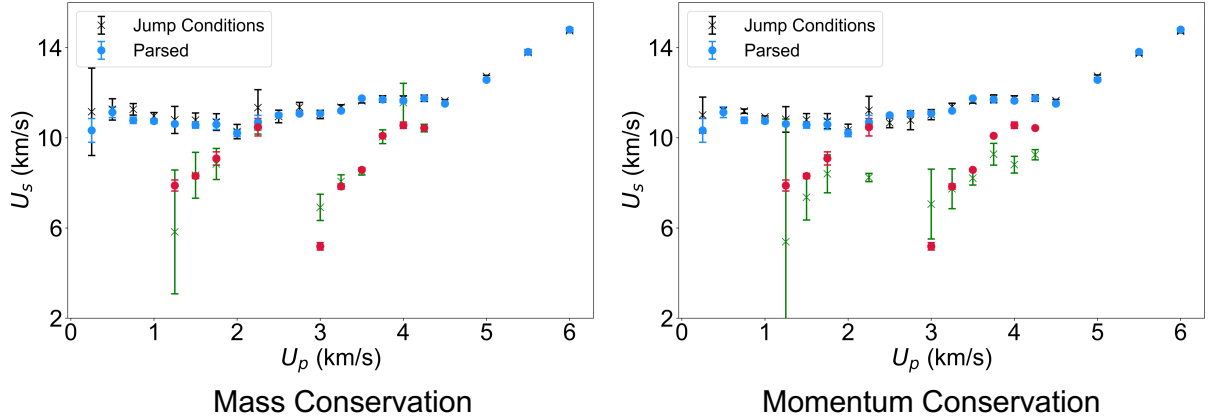


Figure 7: Comparing parsed u_s with the values calculated from the Rankine-Hugoniot jump conditions. The error bars for the jump conditions are obtained using error propagation.

workflow has been published as an open-source tool on nanoHUB,[26] accessible for online simulations[27], where researchers can analyze their own data. The tool takes the trajectory file and piston velocity as input, along with metadata information such as alias, system, and type of simulation (e.g. “Momentum Mirror”), so that it can be easily retrieved later. It calculates all the properties mentioned above and saves them with the standard deviation in clustering. Everything is stored in a universally indexed database, which also implements caching to avoid data redundancy. This aligns with our goal of making workflows Findable, Accessible, Interoperable, and Reusable (FAIR) for the advancement of the scientific community. The inputs, outputs, and workflow of the tool are highlighted in Figure 8.

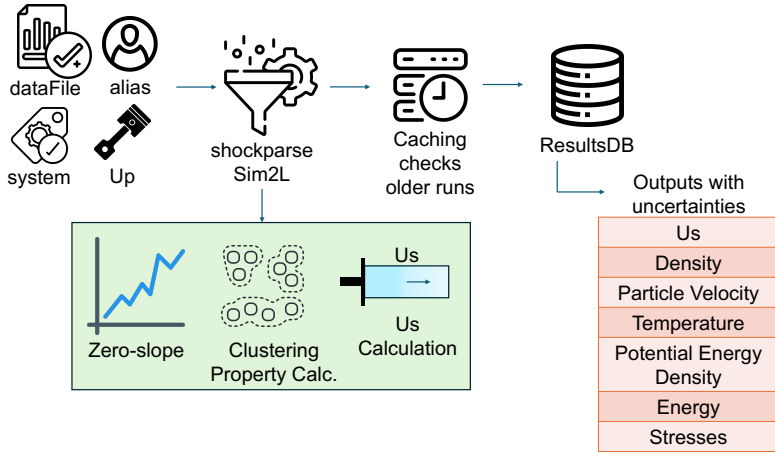


Figure 8: Workflow for the online published tool that saves the results in a universally indexed database for future querying.

3.0.3. Up- U_s Datasets

The final u_s vs. u_p data set is shown in Figure 2 and compared with data available from the literature in Figure 9. The data shows good agreement with past studies, again

highlighting the regimes of interest comprised of the three branches: elastic wave, plastic wave, and phase transformation wave. The plastic wave begins to show at particle velocity around $u_p = 1.25$ km/s. Its propagation speed increases with increasing particle velocity until the particle velocity reaches $u_p = 2.5$ km/s. The phase transformation wave starts when the particle velocity is slightly higher than $u_p = 2.5$ km/s. Its propagation speed also increases with increasing particle velocity until the particle velocity reaches $u_p = 4.25$ km/s. When the particle velocity is above $u_p = 4.5$ km/s, there is a single overdriven wave, whose propagation speed shows a linear increase with particle velocity.

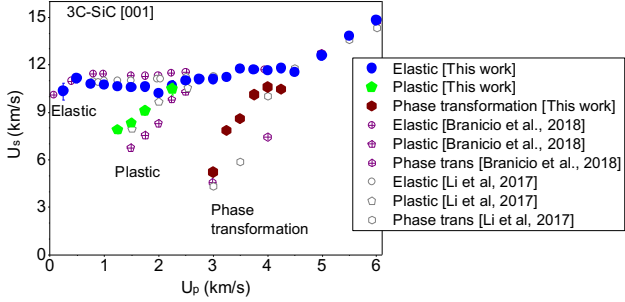


Figure 9: Shock velocity versus particle velocity from this work compared with previous results.

4. Physics-constrained Gaussian Process for Shock State Prediction

4.1. Gaussian Process regression

Before deriving and presenting the proposed model, the essentials of Gaussian process regression (GPR) are introduced here, upon which the model presented in Section 4 will be developed.

GPR is a non-parametric kernel-based regression that assumes the output variables follow a Gaussian stochastic process indexed on the set of input variables. The approach leverages a small number of hyper-parameters to define a learnable correlation structure for the stochastic process, providing a measurable degree of confidence in the predictions [14].

A GP, $Y(\mathbf{x})$, is a collection of random variables indexed on the input vector \mathbf{x} such that, for any pair of inputs \mathbf{x} and \mathbf{x}' , the pair of random variables $Y(\mathbf{x}), Y(\mathbf{x}')$ follows a joint normal distribution. As a result, a GP can be completely defined by its mean function $\mu(\mathbf{x})$ and positive-definite covariance function $K(\mathbf{x}, \mathbf{x}')$. Given a set of training data $\{\mathbf{x}^{(i)}, y^{(i)}\}_{i=1}^N$ with $\mathbf{X} = [\mathbf{x}^{(1)}, \dots, \mathbf{x}^{(N)}]^\top$ and $\mathbf{y} = [y^{(1)}, \dots, y^{(N)}]^\top$ the GP prior is written as

$$Y(\mathbf{x}) \sim \mathcal{GP}(\mu(\mathbf{x}), K(\mathbf{x}, \mathbf{x}')) \quad (12)$$

where $\mu(\mathbf{x})$ is defined using a polynomial fit based on the input vector \mathbf{x} . A popular choice for the covariance function is the squared exponential (radial basis function) kernel with additive white noise given by,

$$K(\mathbf{x}, \mathbf{x}') = \sigma^2 \exp\left(-\frac{\|\mathbf{x}-\mathbf{x}'\|^2}{2\ell^2}\right) + \sigma_n^2 \delta_{\mathbf{x}, \mathbf{x}'} \quad (13)$$

where ℓ is the length-scale, σ^2 the signal variance, and σ_n^2 the noise variance. The hyper-parameters are collected in the vector $\boldsymbol{\theta} = \{\ell, \sigma, \sigma_n\}$.

Let the kernel matrix be $\mathbf{K} = [K(\mathbf{x}^i, \mathbf{x}^j)]_{i,j=1}^N$ and define the kernel entry $k(\mathbf{x}^*) = [K(\mathbf{x}^{(1)}, \mathbf{x}^*), \dots, K(\mathbf{x}^{(N)}, \mathbf{x}^*)]^\top$. For a new input \mathbf{x}^* the posterior prediction conditioned on the training data \mathbf{X}, \mathbf{y} is Gaussian, and denoted by

$$Y(\mathbf{x}^*) | \mathbf{y}, \mathbf{X}, \mathbf{x}^* \sim \mathcal{N}(m(\mathbf{x}^*), s^2(\mathbf{x}^*)) \quad (14)$$

with posterior mean

$$m(\mathbf{x}^*) = \mu(\mathbf{x}^*) + k(\mathbf{x}^*)^\top K^{-1}(\mathbf{y} - \boldsymbol{\mu}) \quad (15)$$

and posterior variance

$$s^2(\mathbf{x}^*) = K(\mathbf{x}^*, \mathbf{x}^*) - k(\mathbf{x}^*)^\top K^{-1}k(\mathbf{x}^*) \quad (16)$$

where $\boldsymbol{\mu} = [\mu(\mathbf{x}^{(1)}), \dots, \mu(\mathbf{x}^{(N)})]^\top$.

The hyper-parameters, $\boldsymbol{\theta}$, are usually inferred via a maximum-a-posteriori (MAP) estimate. With a Gaussian prior $\boldsymbol{\theta} \sim \mathcal{N}(\boldsymbol{\mu}_\theta, \Sigma_\theta)$, the MAP estimate is given by

$$\hat{\boldsymbol{\theta}}_{\text{MAP}} = \arg \min_{\boldsymbol{\theta}} \left[-\log p(\mathbf{y} | \mathbf{X}, \boldsymbol{\theta}) - \log p(\boldsymbol{\theta}) \right] \quad (17)$$

where the negative log-likelihood term can be expressed as

$$-\log p(\mathbf{y} | \mathbf{X}, \boldsymbol{\theta}) = \frac{1}{2} \left[(\mathbf{y} - \boldsymbol{\mu})^\top K^{-1}(\mathbf{y} - \boldsymbol{\mu}) + \log|K| + N \log(2\pi) \right] \quad (18)$$

and the negative log-prior can be written as

$$-\log p(\boldsymbol{\theta}) = \frac{1}{2} \left[(\boldsymbol{\theta} - \boldsymbol{\mu}_\theta)^\top \Sigma_\theta^{-1} (\boldsymbol{\theta} - \boldsymbol{\mu}_\theta) + \log|\Sigma_\theta| + d \log(2\pi) \right] \quad (19)$$

In the next section, the constrained Gaussian process model for shock state prediction is derived and fully formulated. First, the necessary thermodynamic constraints for the model are presented. Then, a GP model that is consistent with the generalized Rankine-Hugoniot conditions from Section 2.1 is derived.

4.2. Thermodynamic Constraints

The model aims to predict the thermodynamic state variables (P, V, T) along with the shock velocity for a given piston velocity. Importantly, these state variables must satisfy the laws of thermodynamics. These are distinguished into two conditions. The first constraint is the thermodynamic consistency condition, which establishes a relationship between the thermodynamic variables through a single variable known as the Helmholtz free energy, F , defined as

$$F = E - TS \quad (20)$$

where S denotes the entropy. The first law of thermodynamics states that changes in the free energy are given in the differential form $dF = -SdT - PdV$. Thus, the pressure and energy can be related to the Helmholtz free energy by

$$P = -\left. \frac{\partial F}{\partial V} \right|_T, \quad E = F - T \left. \frac{\partial F}{\partial T} \right|_V \quad (21)$$

Taking the derivatives $\partial P/\partial T$ and $\partial E/\partial V$ yields the thermodynamic consistency constraint

$$P = T \frac{\partial P}{\partial T} - \frac{\partial E}{\partial V} \quad (22)$$

The second thermodynamic constraint, also known as thermodynamic stability, is obtained from the second law of thermodynamics, which requires convexity of the Helmholtz free energy with respect to the thermodynamic variables. As a result, the specific heat (c_V) and isothermal compressibility (κ_T) are positive quantities. This is consistent with the expectation that energy must be added to the system to raise its temperature and that an increase in pressure decreases the volume. In this regard, the thermodynamic stability constraints are given as

$$\left(\frac{\partial^2 S}{\partial E^2} \right)_V = -\frac{1}{T^2} \left(\frac{\partial T}{\partial E} \right)_V = \frac{1}{T^2 c_V} \leq 0 \iff \left(\frac{\partial T}{\partial E} \right)_V \geq 0 \quad (23)$$

$$\left(\frac{\partial^2 F}{\partial V^2} \right)_T = -\left(\frac{\partial P}{\partial V} \right)_T = \frac{1}{V \kappa_T} \geq 0 \iff \left(\frac{\partial P}{\partial V} \right)_T \leq 0 \quad (24)$$

Clearly, a GP formulation that satisfies the generalized Hugoniot jump conditions in Eqs. (6), (8)-(9) should also be consistent with these thermodynamic constraints. In this regard, from the maximal set of all possible hyperparameters, $\boldsymbol{\theta}$, in Eq. (13), a thermodynamically consistent subset is identified by enforcing the equality constraint in Eq. (22) and the inequalities in Eqs. (23) and (24).

4.3. Rankine-Hugoniot-based Gaussian process formulation

In this section, a GP model for shock relations following the Rankine-Hugoniot conditions in Eqs. (6), (8)-(9) is presented. First, a GP prior is placed on the two dependent variables $u_{s_i}(u_p)$ and $\nu_{z_i}(u_p)$ as

$$\mathbf{X} = \{u_{s_i}; \nu_{z_i}\} \sim \mathcal{GP}\left(\boldsymbol{\mu}(u_p), \mathbf{K}(u_p, u'_p)\right) \quad (25)$$

where $\boldsymbol{\mu}(u_p)$ and $\mathbf{K}(\cdot, \cdot)$ are the mean vector and covariance (kernel) function for the outputs $\{u_{s_i}, \nu_{z_i}\}$. The cross-covariances are defined using the squared-exponential kernel in Eq. (13) where $\boldsymbol{\mu}(u_p)$ and $\mathbf{K}(\cdot, \cdot)$ denote the mean vector and covariance (kernel) function for the outputs $\{u_{s_i}, \nu_{z_i}\}$. The auto- and cross-covariances are defined using the squared-exponential kernel in Eq. (13) as

$$\begin{aligned} K_{u_s u_s}(u_p, u_p) &= \sigma_{u_s}^2 k(u_p, u_p) + \sigma_{n, u_s}^2 \delta_{u_p, u_p} \\ K_{v_z v_z}(u_p, u_p) &= \sigma_{v_z}^2 k(u_p, u_p) + \sigma_{n, v_z}^2 \delta_{u_p, u_p} \\ K_{u_s v_z}(u_p, u_p) &= \rho \sigma_{u_s} \sigma_{v_z} k(u_p, u_p) \end{aligned} \quad (26)$$

These covariance components can be compactly expressed through the intrinsic coregionalization model (ICM) [28], where the joint covariance is written as

$$\mathbf{K}(u_p, u_p) = \mathbf{B} \otimes k(u_p, u_p) + \mathbf{D} \quad (27)$$

where \otimes denotes the Kronecker product, \mathbf{D} is a diagonal matrix whose (l, l) -th element is the observation noise variance $\sigma_{n,l}^2$ for the l -th output, and \mathbf{B} is a positive semidefinite coregionalization matrix given by

$$\mathbf{B} = \begin{bmatrix} \sigma_{u_s}^2 & \rho \sigma_{u_s} \sigma_{v_z} \\ \rho \sigma_{u_s} \sigma_{v_z} & \sigma_{v_z}^2 \end{bmatrix} \quad (28)$$

where σ_{u_s} and σ_{v_z} are the marginal standard deviations of u_s and v_z , respectively, and ρ is their correlation coefficient ($-1 < \rho < 1$). Both outputs share a common squared-exponential kernel

$$k(u_p, u_p) = \exp\left[-\frac{(u_p - u_p)^2}{2\ell^2}\right] \quad (29)$$

with a single characteristic length scale ℓ . The resulting model depends on a set of four hyperparameters, collected in the vector $\boldsymbol{\theta} = \{\sigma_{u_s}, \sigma_{v_z}, \rho, \ell\}$. To ensure thermodynamic consistency with the generalized Rankine-Hugoniot conditions in Eqs. (6), (8)-(9) and the thermodynamic consistency and stability conditions in Eqs. (22)–(24), we need to consider the following set of augmented outputs,

$$\mathbf{Y} = \begin{pmatrix} u_{s_i} \\ v_{z_i} \\ P_i \\ \rho_i \\ T_i \end{pmatrix} \quad (30)$$

For these augmented outputs, we define a joint GP prior by

$$\mathbf{Y} \mid u_p \sim \mathcal{GP}(\boldsymbol{\mu}, \boldsymbol{\Sigma}) \quad (31)$$

where $\boldsymbol{\mu}$ is the mean vector for each component of \mathbf{Y} , and $\boldsymbol{\Sigma}$ is the block covariance matrix:

$$\boldsymbol{\Sigma} = \begin{pmatrix} K_{u_{s_i}, u_{s_i}} & K_{u_{s_i}, v_{z_i}} & K_{u_{s_i}, P_i} & K_{u_{s_i}, \rho_i} & K_{u_{s_i}, T_i} \\ K_{v_{z_i}, u_{s_i}} & K_{v_{z_i}, v_{z_i}} & K_{v_{z_i}, P_i} & K_{v_{z_i}, \rho_i} & K_{v_{z_i}, T_i} \\ K_{P_i, u_{s_i}} & K_{P_i, v_{z_i}} & K_{P_i, P_i} & K_{P_i, \rho_i} & K_{P_i, T_i} \\ K_{\rho_i, u_{s_i}} & K_{\rho_i, v_{z_i}} & K_{\rho_i, P_i} & K_{\rho_i, \rho_i} & K_{\rho_i, T_i} \\ K_{T_i, u_{s_i}} & K_{T_i, v_{z_i}} & K_{T_i, P_i} & K_{T_i, \rho_i} & K_{T_i, T_i} \end{pmatrix} \quad (32)$$

The sub-blocks of $\boldsymbol{\Sigma}$ associated with the auto-covariances and cross-covariances of P_i , ρ_i , and T_i are computed from the generalized Rankine-Hugoniot relations in Eqs. (6), (8)–(9) using a Taylor series expansion around the mean vector $\bar{\mathbf{x}} = \{\bar{u}_{s_i}, \bar{v}_{z_i}\}$ (i.e. the Delta method [29]) and considering known values for the state variables ahead of the shock wave, i.e., $v_{z_{i-1}}, \rho_{i-1}, P_{i-1}, T_{i-1}, E_{i-1}$.

Specifically, for a scalar-valued function $f : \mathbb{R}^n \rightarrow \mathbb{R}$, expanded around a point $\mathbf{a} \in \mathbb{R}^n$, the second-order Taylor series up to second order is

$$T(\mathbf{x}) = f(\mathbf{a}) + (\mathbf{x} - \mathbf{a})^\top \nabla f(\mathbf{a}) + \frac{1}{2}(\mathbf{x} - \mathbf{a})^\top \mathbf{H}(\mathbf{a})(\mathbf{x} - \mathbf{a}) + \mathcal{O}(\|\mathbf{x} - \mathbf{a}\|^3) \quad (33)$$

where

$$\nabla f(\mathbf{a}) = \begin{pmatrix} \frac{\partial f}{\partial x_1} \Big|_{\mathbf{a}} \\ \frac{\partial f}{\partial x_2} \Big|_{\mathbf{a}} \\ \vdots \\ \frac{\partial f}{\partial x_n} \Big|_{\mathbf{a}} \end{pmatrix}, \quad \mathbf{H}(\mathbf{a}) = \begin{pmatrix} \frac{\partial^2 f}{\partial x_1^2} \Big|_{\mathbf{a}} & \frac{\partial^2 f}{\partial x_1 \partial x_2} \Big|_{\mathbf{a}} & \cdots & \frac{\partial^2 f}{\partial x_1 \partial x_n} \Big|_{\mathbf{a}} \\ \frac{\partial^2 f}{\partial x_2 \partial x_1} \Big|_{\mathbf{a}} & \frac{\partial^2 f}{\partial x_2^2} \Big|_{\mathbf{a}} & \cdots & \frac{\partial^2 f}{\partial x_2 \partial x_n} \Big|_{\mathbf{a}} \\ \vdots & \vdots & \ddots & \vdots \\ \frac{\partial^2 f}{\partial x_n \partial x_1} \Big|_{\mathbf{a}} & \frac{\partial^2 f}{\partial x_n \partial x_2} \Big|_{\mathbf{a}} & \cdots & \frac{\partial^2 f}{\partial x_n^2} \Big|_{\mathbf{a}} \end{pmatrix} \quad (34)$$

and the term $\mathcal{O}(\|\mathbf{x} - \mathbf{a}\|^3)$ denotes terms higher than second order.

Consider that there exist N input-output data points consisting of $\mathbf{u}_p = \{u_p^j\}_{j=1}^N$ and \mathbf{Y} having components $\mathbf{y}^j = \{u_{s_i}^j, \nu_{z_i}^j, P_i^j, \rho_i^j, T_i^j\}$ such that the Kernel functions of the block covariance matrix in Eq. (32) are expressed as $N \times N$ matrices \mathbf{K}_{lm} with $l, m = 1, \dots, 5$ indexing the components of \mathbf{Y} . For brevity, the Hugoniot functions in Eqs. (6), (8)–(9), (33) are written as functions $y_l = f_l(u_{s_i}, \nu_{z_i}; \nu_{z_{i-1}})$ where again l indexes the terms of \mathbf{y} such that, e.g. $y_3 = P_i$. This is justified in [Appendix B](#) where it is shown that each of the Rankine-Hugoniot equations can indeed be written in this manner. Taking the Taylor series expansion of this abstracted function, the expectation operation $\mathbb{E}[\cdot]$ is applied over the random variable, which yields the following mean value for the j^{th} data point:

$$\begin{aligned} \bar{y}_l^j &= \mathbb{E}[y_l^j] = f_l(\bar{u}_{s_i}^j, \bar{\nu}_{z_i}^j; \nu_{z_{i-1}}^j) \\ &+ \frac{1}{2} \left[\frac{\partial^2 f_l}{\partial (u_{s_i})^2} \Big|_{\bar{\mathbf{x}}^j} \mathbf{K}_{u_{s_i} u_{s_i}}^{jj} + \frac{\partial^2 f_l}{\partial (\nu_{z_i})^2} \Big|_{\bar{\mathbf{x}}^j} \mathbf{K}_{\nu_{z_i} \nu_{z_i}}^{jj} \right. \\ &\quad \left. + 2 \frac{\partial^2 f_l}{\partial u_{s_i} \partial \nu_{z_i}} \Big|_{\bar{\mathbf{x}}^j} \mathbf{K}_{u_{s_i} \nu_{z_i}}^{jj} \right] \end{aligned} \quad (35)$$

Likewise, the abstracted covariance between the j^{th} and k^{th} data points of the l^{th} and m^{th} output variables is given by

$$\begin{aligned} K(y_l^j, y_m^k) &= \mathbb{E}[y_l^j y_m^k] - \mathbb{E}[y_l^j] \mathbb{E}[y_m^k] \\ &\approx \frac{\partial f_l}{\partial u_{s_i}} \Big|_{\bar{\mathbf{x}}^j} \frac{\partial f_m}{\partial u_{s_i}} \Big|_{\bar{\mathbf{x}}^k} \mathbf{K}_{u_{s_i} u_{s_i}}^{jk} \\ &\quad + \left(\frac{\partial f_l}{\partial u_{s_i}} \Big|_{\bar{\mathbf{x}}^j} \frac{\partial f_m}{\partial \nu_{z_i}} \Big|_{\bar{\mathbf{x}}^k} + \frac{\partial f_l}{\partial \nu_{z_i}} \Big|_{\bar{\mathbf{x}}^j} \frac{\partial f_m}{\partial u_{s_i}} \Big|_{\bar{\mathbf{x}}^k} \right) \mathbf{K}_{u_{s_i} \nu_{z_i}}^{jk} \\ &\quad + \frac{\partial f_l}{\partial \nu_{z_i}} \Big|_{\bar{\mathbf{x}}^j} \frac{\partial f_m}{\partial \nu_{z_i}} \Big|_{\bar{\mathbf{x}}^k} \mathbf{K}_{\nu_{z_i} \nu_{z_i}}^{jk} \end{aligned} \quad (36)$$

The complete derivation for this covariance can be found in [Appendix A](#). Further, the final expressions for the mean values and each block term of Σ can be found in [Appendix C](#) using the analytical derivatives from [Appendix B](#).

Note that the augmented output vector \mathbf{Y} contains temperature T rather than internal energy E . As outlined in Section 2, temperature measurements are not typically available in shock experiments in which the specific heat $C_v(T)$ is not readily available. To address this limitation, a linear temperature-energy relationship is assumed following the form

$$T_i = a + bE_i \quad (37)$$

with covariance function expressed as

$$K_{T_i T_i}^{jk} \approx b^2 K_{E_i E_i}^{jk} \quad (38)$$

Likewise, the cross-covariances for temperature can be computed in a similar fashion as shown in [Appendix C](#).

Each distinct sub-block of the full covariance matrix in Eq. (32) can be expressed in compact form using the intrinsic coregionalization approach. Specifically, using Eqs. (28) and (29), the covariance term in Eq. (36) for a pair of outputs y_l and y_m can be written as

$$\mathbf{K}_{lm} = \mathbf{L}_{lm}^T (\mathbf{B} \otimes k(u_p, u_p)) \mathbf{L}_{lm} + \mathbf{D}_{lm} \quad (39)$$

where \mathbf{L}_{lm} contains the first-order derivatives of the variables $f_l(\cdot)$ and $f_m(\cdot)$ with respect to the GP variables $\{u_{s_i}, \nu_{z_i}\}$, as defined in Eq. (36), \mathbf{B} is the coregionalization matrix from Eq. (28), and \mathbf{D}_{lm} is a diagonal matrix containing the observation noise variances for each output pair. The complete joint covariance matrix in Eq. (32) can be compactly represented as the Kronecker product

$$\boldsymbol{\Sigma} = \mathbf{L}^T (\mathbf{B} \otimes k(u_p, u_p)) \mathbf{L} + \mathbf{D} \quad (40)$$

where \mathbf{L} contains the first-order derivative terms from the Taylor expansion. Considering that both \mathbf{B} and \mathbf{K}_{u_p, u_p} are positive semidefinite, their Kronecker product is also positive semidefinite, and multiplication by \mathbf{L}^T and \mathbf{L} preserves this property. Since \mathbf{D} is diagonal with nonnegative entries, it is positive semidefinite, and the sum of two positive semidefinite matrices remains positive semidefinite. This structured representation enforces joint positive semidefiniteness of $\boldsymbol{\Sigma}$, thus improving numerical stability and mitigating matrix-invertibility issues that often arise in physics-constrained Gaussian Processes.

Furthermore, it can be ensured that the derived GP model satisfies the thermodynamic consistency and stability constraints in Eqs. (22)–(24). For the pressure stability constraint in Eq. (8), the chain rule is applied as follows to show that, if the model satisfies the Rankine-Hugoniot equations (specifically Eq. (8)), the stability constraint is automatically satisfied:

$$\frac{\partial P_i^j}{\partial V_i^j} = \frac{\partial P_i^j}{\partial \nu_{z_i}^j} \cdot \frac{\partial \nu_{z_i}^j}{\partial V_i^j} = \frac{\partial P_i^j / \partial \nu_{z_i}^j}{\partial V_i^j / \partial \nu_{z_i}^j} = -(\rho_i^j)^2 (u_{s_i}^j - \nu_{z_i}^j)^2 < 0 \quad (41)$$

Next, considering the linear model for temperature in Eq. (37), differentiation with respect to E_i^j yields

$$\frac{\partial T_i^j}{\partial E_i^j} = b \quad (42)$$

and the consistency constraint in Eq. (24) is expressed as

$$\frac{\partial E_i^j}{\partial T_i^j} = \frac{1}{b} \quad (43)$$

Therefore, to ensure thermodynamic stability according to Eq. (24), the polynomial coefficients (a, b) are obtained by solving the following constrained optimization problem:

$$\min_{a,b} \sum_{k=1}^N (T_i^k - (a + bE_i^k))^2, \quad \text{subject to } b > \varepsilon \quad \forall k \quad (44)$$

Next, the model is trained using the input and the MD-generated vector of augmented outputs \mathbf{Y} to obtain the hyperparameters $\boldsymbol{\theta}$ of the GP model using Eq. (17). From a practical perspective, a straightforward use of the cross-covariance from Eq. (32) leads to numerical instabilities as a result of poor relative scaling. In fact, physics-constrained GP models with multiple-outputs are known to suffer from positive definiteness issues [30]. In this work, the values associated with u_s and T , for example, differ by several orders of magnitude such that $\max(u_s)/\min(T) \sim \mathcal{O}(10^{-4})$, leading to large dynamic ranges across the sub-block covariances in Eq. (32). Furthermore, the analytical derivatives, which can dominate the overall magnitude of Eq. (36), lead to large dynamic ranges within the sub-block covariance terms. For example, $\min(\mathbf{K}_{T_i, T_i})/\max(\mathbf{K}_{T_i, T_i}) \sim \mathcal{O}(10^{-8})$. These scaling discrepancies result in $\boldsymbol{\Sigma}$ being ill-conditioned and non-invertible. These issues are mitigated using a linear transformation of the diagonal elements of the Hessian such that they are approximately equal to one [31].

To ensure numerical stability, the following coordinate transformation is employed

$$\tilde{P}_i = s_1 P_i, \quad \tilde{\rho}_i = s_1 \rho_i, \quad \tilde{T}_i = s_2 T_i \quad (45)$$

where s_1, s_2 are inversely proportional to the maximum values of $\{P_i, \rho_i\}$ and T_i , respectively. It is readily seen that the original structure of the Rankine-Hugoniot conditions is preserved when using the scaling in Eq. (45). For practical purposes, training is then performed to obtain the optimal hyperparameters $\boldsymbol{\theta}$ using the scaled augmented output $\tilde{\mathbf{Y}} = \{u_{s_i}, \nu_{z_i}, \tilde{P}_i, \tilde{\rho}_i, \tilde{T}_i\}^\top$ using gradient-based algorithms [32], although for clarity of the formulation the GP model is presented in terms of unscaled quantities.

For a given set of testing points $\mathbf{u}_p^* = \{u_p^j\}_{j=1}^M$ the predictive distribution of the joint GP model for the values $\mathbf{Y}^* = \{u_{s_i}^*, \nu_{z_i}^*, P_i^*, \rho_i^*, T_i^*\}^\top$ is calculated as a joint Gaussian distribution across the training and test data points given by

$$\mathbf{Y}^* \mid \mathbf{u}_p, \mathbf{Y}, \mathbf{u}_p^* \sim \mathcal{GP} \left(\begin{bmatrix} \boldsymbol{\mu}(\mathbf{u}_p) \\ \boldsymbol{\mu}(\mathbf{u}_p^*) \end{bmatrix}, \begin{bmatrix} \boldsymbol{\Sigma}(\mathbf{u}_p, \mathbf{u}_p) & \boldsymbol{\Sigma}(\mathbf{u}_p, \mathbf{u}_p^*) \\ \boldsymbol{\Sigma}(\mathbf{u}_p^*, \mathbf{u}_p) & \boldsymbol{\Sigma}(\mathbf{u}_p^*, \mathbf{u}_p^*) \end{bmatrix} \right) \quad (46)$$

Conditioning on the training data gives the posterior predictive distribution as

$$\mathbf{Y}^* \mid \mathbf{u}_p, \mathbf{Y}, \mathbf{u}_p^* \sim \mathcal{GP} \left(\begin{bmatrix} \boldsymbol{\mu}(\mathbf{u}_p^*) + \boldsymbol{\Sigma}(\mathbf{u}_p^*, \mathbf{u}_p) \boldsymbol{\Sigma}(\mathbf{u}_p, \mathbf{u}_p)^{-1} (\mathbf{Y} - \boldsymbol{\mu}(\mathbf{u}_p)) \\ \boldsymbol{\Sigma}(\mathbf{u}_p^*, \mathbf{u}_p^*) - \boldsymbol{\Sigma}(\mathbf{u}_p^*, \mathbf{u}_p) \boldsymbol{\Sigma}(\mathbf{u}_p, \mathbf{u}_p)^{-1} \boldsymbol{\Sigma}(\mathbf{u}_p, \mathbf{u}_p^*) \end{bmatrix} \right) \quad (47)$$

Note that in both Eq. (46) and (47) explicit dependence on u_p is shown, but we emphasize that much of the covariance structure depends on u_p only through $\{u_{s_i}, \nu_{z_i}\}$ as explained following Eq. (32). Moreover, the specific block covariances in Σ are computed as detailed above and in [Appendix A](#)

5. Results and Discussion

In this section, the proposed physics-constrained GP model is demonstrated for predicting shock velocities and state variables for single crystal SiC-3C shocked along the [001] crystallographic orientation. The model is trained using $N = 21$ MD shock simulations, as described in Section 3.

The simulation data are shown in Fig. 2 and described in detail in Section 2. To account for the multi-wave structure of the shock propagation, three distinct GP models are constructed for the leading wave, plastic wave, and phase transformation wave. This is achieved by partitioning the data into three mutually inclusive training data sets comprised of u_p and the corresponding augmented state vectors from Eq. (30) from the respective wave. We note that the data sets are mutually inclusive because as trailing waves increase in velocity (at higher u_p), they merge with the leading wave. The corresponding data points are included in both the leading wave model and the corresponding plastic or phase transformation wave model. For example, the data point having $u_p = 2.75$ km/s in Figure 2 is both the leading wave and a plastic wave.

First, the leading-wave GP model, denoted by $\mathcal{GP}_{\text{lead}}$, is trained on all data points shown in blue in Figure 2. Next, the plastic wave GP model, denoted by \mathcal{GP}_{pl} , is trained on the set of red data points (corresponding to the trailing plastic wave) plus the subset of blue data points having $u_p > 2.25$ km/s for which the leading wave is no longer elastic. Finally, the phase transformation GP model, denoted by \mathcal{GP}_{pt} , is trained on the set of green data points (corresponding to the trailing phase transformation wave) plus the subset of blue data points having $u_p > 4.25$ km/s corresponding to the overdriven region where a phase transformation occurs in the leading wave.

The three GP models are trained sequentially to account for the multi-wave structure using the generalized (multi-wave) Hugoniot equations in Eq. (6), Eq. (8)-(9). First, $\mathcal{GP}_{\text{lead}}$ is trained such that $\nu_{z_{i-1}}, \rho_{i-1}, P_{i-1}, T_{i-1}, E_{i-1}$ take values associated with the ambient material state ahead of the shock $\nu_{z_0} = 0, \rho_0, P_0, T_0, E_0$. Predictions are made for u_{s_1} and the state variables $\nu_{z_1}, \rho_1, P_1, T_1, E_1$ in the material behind the leading wave.

Next, \mathcal{GP}_{pl} is trained such that, when the plastic wave trails a leading elastic wave, $\mathcal{GP}_{\text{lead}}$ is used to predict the material state ahead of the wave. That is, $\nu_{z_{i-1}}, \rho_{i-1}, P_{i-1}, T_{i-1}, E_{i-1}$ take the values of $\nu_{z_1}, \rho_1, P_1, T_1, E_1$ predicted from $\mathcal{GP}_{\text{lead}}$. When the plastic wave is the leading wave, the state variables ahead of the wave once again take values associated with the ambient material state $\nu_{z_0} = 0, \rho_0, P_0, T_0, E_0$. Predictions are then made for u_{s_i} and the state variables $\nu_{z_i}, \rho_i, P_i, T_i, E_i$ in the material behind the plastic wave, where $i = 2$ in a multi-wave structure when the plastic wave trails and $i = 1$ when the plastic wave leads.

Finally, the same procedure is followed for training \mathcal{GP}_{pt} such that predictions from \mathcal{GP}_{pl} are used for the material state ahead of the wave when it trails the plastic wave and the ambient state is applied ahead of the wave in the overdriven regime.

The resulting GP predictions are shown in Figures 10–14. Figure 10 shows the GP predictions for each shock wave velocity, u_s , where the blue curve shows the leading wave with 95% confidence interval, the red curve shows the plastic wave with 95% confidence interval, and the green curve shows the phase transformation wave with 95% confidence interval. Notice that, as expected, the leading (elastic) and plastic shock velocities converge near $u_p = 2.5$ km/s. Similarly, the leading (plastic) and phase transformations converge near $u_p = 4.5$ km/s. However, the uncertainties associated with each shock velocity differ. For example, the phase transformation wave has considerably higher prediction uncertainty, which implies that it is more difficult to measure from MD simulations (having higher noise) and that there is a higher degree of uncertainty in predicting when the material will reach an overdriven state (i.e. when the phase transformation wave becomes the leading wave).

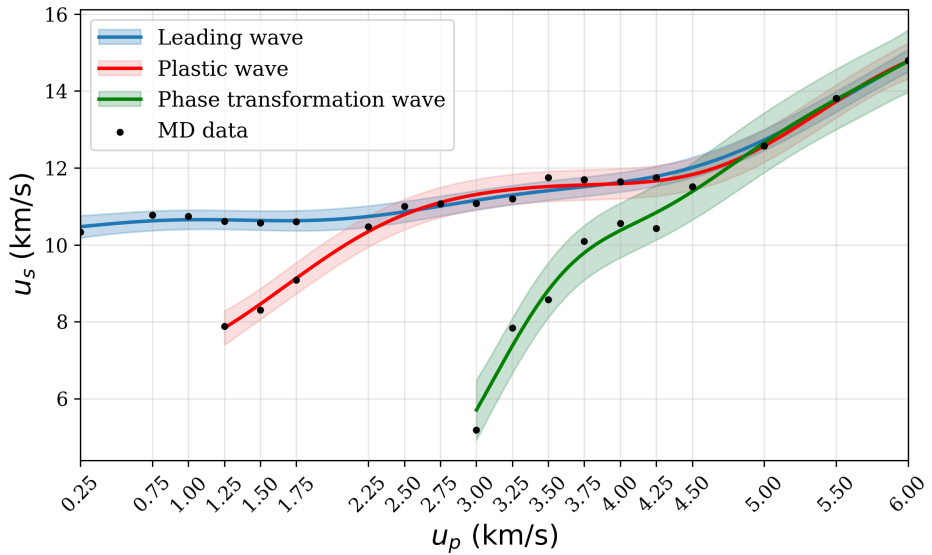


Figure 10: GP predictions of the $u_s - u_p$ relationships for the leading (blue), plastic (red), and phase transition (green) waves. The solid lines represent the mean values and the shaded regions indicate the 95% confidence intervals.

Next, Figure 11 shows the GP prediction for the pressure trailing each wave. Notice here that the pressure trailing the leading wave drops slightly when a trailing (plastic or phase transformation) wave exists, but rises again when the waves merge. The GP model accurately captures this pressure drop as we see the mean leading wave GP has lower pressure than the mean plastic and phase transitions wave GPs when a dual wave structure exists ($u_p \in [1.25, 2.25]$ km/s and $u_p \in [3, 4.25]$ km/s), albeit with significant uncertainties.

Figure 12 shows the GP predicted particle velocities, v_z for each wave. Notice that the trailing wave particle velocity tracks along $v_z = u_p$, because the velocity trailing the final wave must be equal to the piston velocity. However, the particle velocity ahead of the trailing wave must be less than the piston velocity. Therefore, we see that v_z for the leading wave is less than u_p , following a similar trend to the pressure and again captured accurately by the GP model, but introducing significant uncertainty.

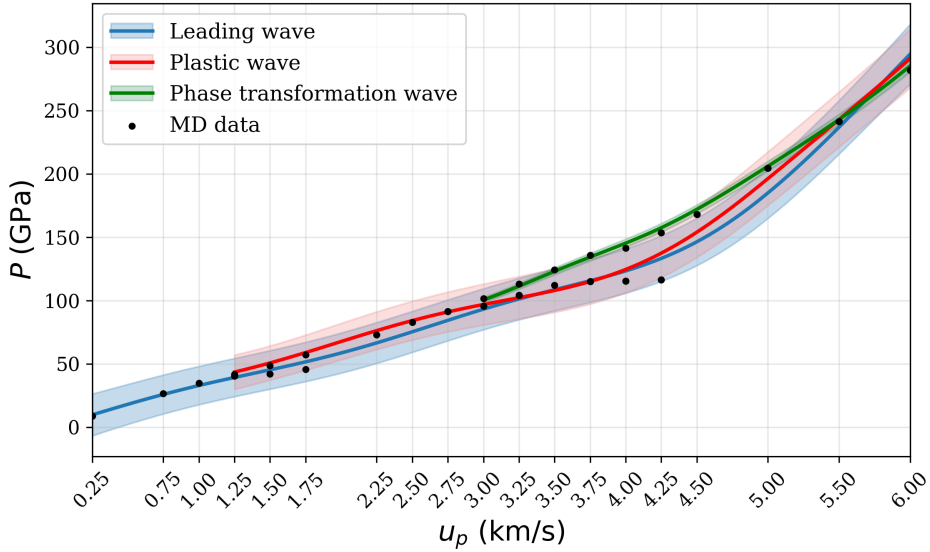


Figure 11: GP predictions for pressure P in the material trailing each wave for the leading (blue), plastic (red), and phase transition (green) waves. The solid lines represent the mean values and the shaded regions indicate the 95% confidence intervals.

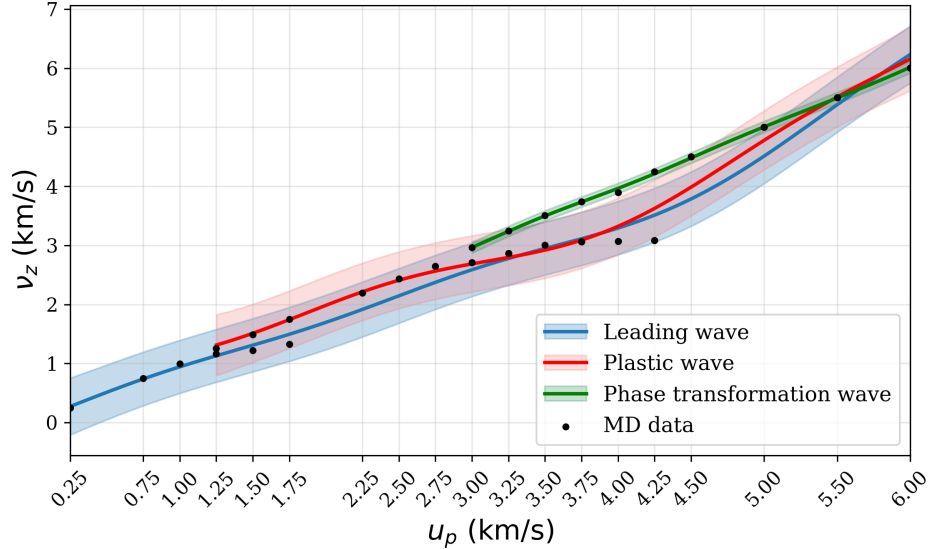


Figure 12: GP predictions for particle velocity v_z , in the material trailing each wave for the leading (blue), plastic (red), and phase transition (green) waves. The solid lines represent the mean values and the shaded regions indicate the 95% confidence intervals.

Figures 13 and 14 show the GP predicted density and temperatures following each wave. Again, we see that density is lower behind the leading wave, and indeed plateaus at a particular value for the training plastic and phase transformation waves. This further implies a sharp increase in trailing density when the trailing and leading waves merge, which the GP

struggles to capture. This is expected as the GP does not adapt well to sudden non-stationary features, instead driving the model toward a smooth solution with large uncertainty. The

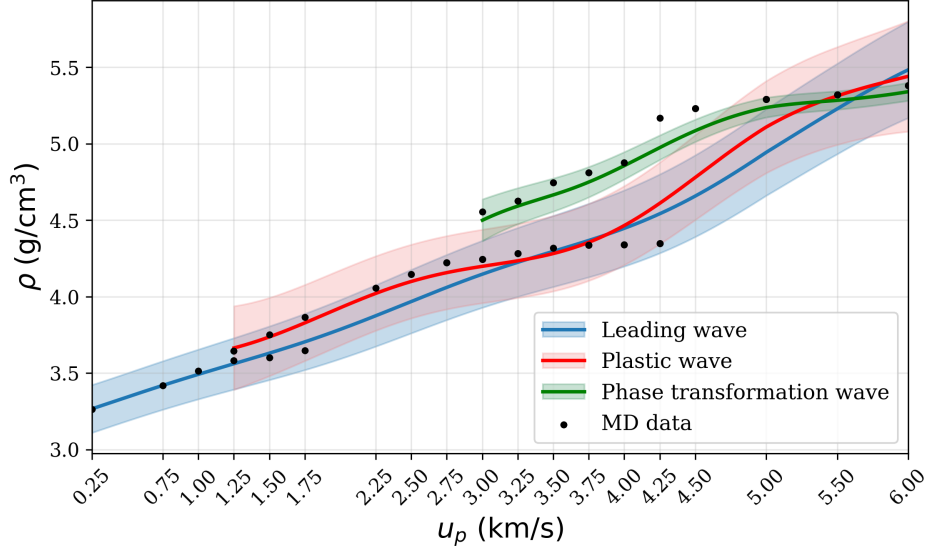


Figure 13: GP predictions for density, ρ in the material trailing each wave for the leading (blue), plastic (red), and phase transition (green) waves. The solid lines represent the mean values and the shaded regions indicate the 95% confidence intervals.

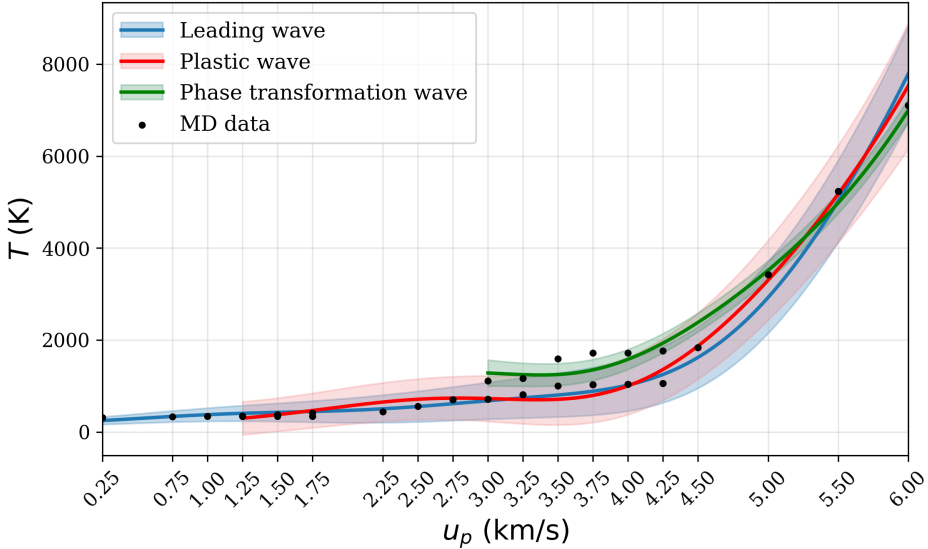


Figure 14: GP predictions for temperature, T in the material trailing each wave for the leading (blue), plastic (red), and phase transition (green) waves. The solid lines represent the mean values and the shaded regions indicate the 95% confidence intervals.

temperature GP meanwhile shows expected trends. It increases gradually for lower particle

velocities with relatively little heat generated from elastic and plastic deformation. However, the phase transformation wave creates significant heat, such that the temperature behind the trailing phase transformation wave is consistently higher than the leading plastic wave. Once in the overdrive regime, heat generation becomes a dominant mechanism for energy dissipation and temperature increases rapidly. Even under the simple temperature assumptions from Eq. (37), the temperature GP accurately represents these phenomena.

Finally, Figures 15 and 16 illustrate the Gaussian Process predictions of the pressure–density and temperature–density Hugoniot states across the elastic, plastic, and phase transformation regimes. We note that the Hugoniot is typically presented in terms of either volume (V) or inverse density ($1/\rho$). The current formulation makes presentation in this way challenging because $1/\rho$, where ρ is Gaussian, follows a strongly non-Gaussian distribution with very heavy tails and undefined mean and variance. To avoid this issue, the GP could be formulated in terms of volume rather than temperature, but providing an alternate formulation is beyond our scope. Nonetheless, we observe the following expected trends. The Hugoniot is a locus of points that results from shocks a different strengths. As such, the data in Figures 15 and 16 are presented such that the mean predictions are shown as dots and the associated uncertainties are shown with ± 2 , std covariance ellipses at each discrete point. In this way, we see that the locus of points that represent the leading wave form a surface whose uncertainty increases for larger shock strengths that generate at higher $\{P, \rho\}$ states. Moreover, the trailing wave states fall below those of the leading wave states, as expected. Interestingly, the covariance ellipses show strong correlation between ρ and P as well as ρ and T . Again, this is expected as even with the large uncertainties in the predictions, we expect that the values of ρ and P, T will increase together.

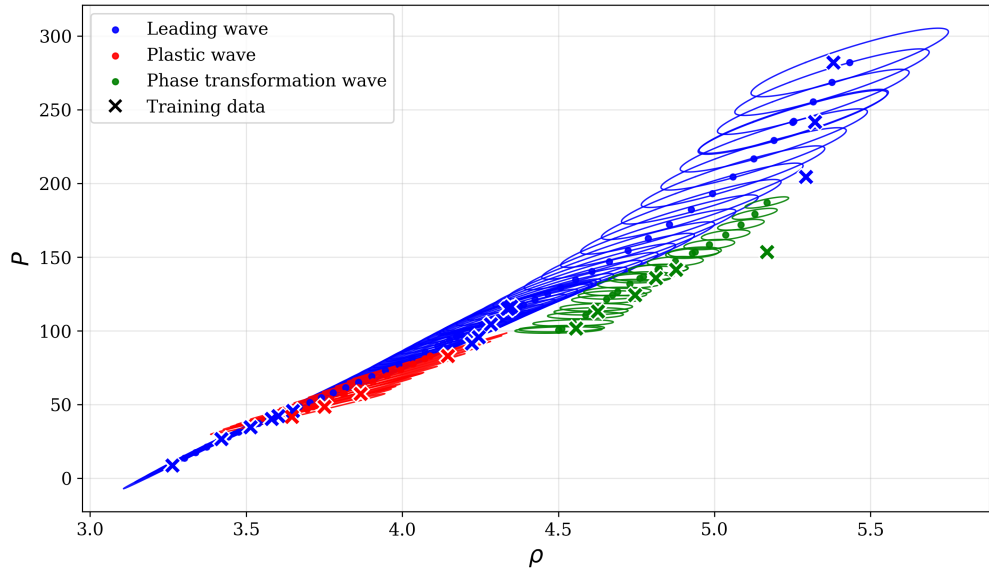


Figure 15: Predicted pressure-density Hugoniot states based on the proposed GP model. The circular markers denote the mean predictions and the ellipses represent ± 2 std constant-probability covariance contours. The crosses indicate the training data used for each wave regime.

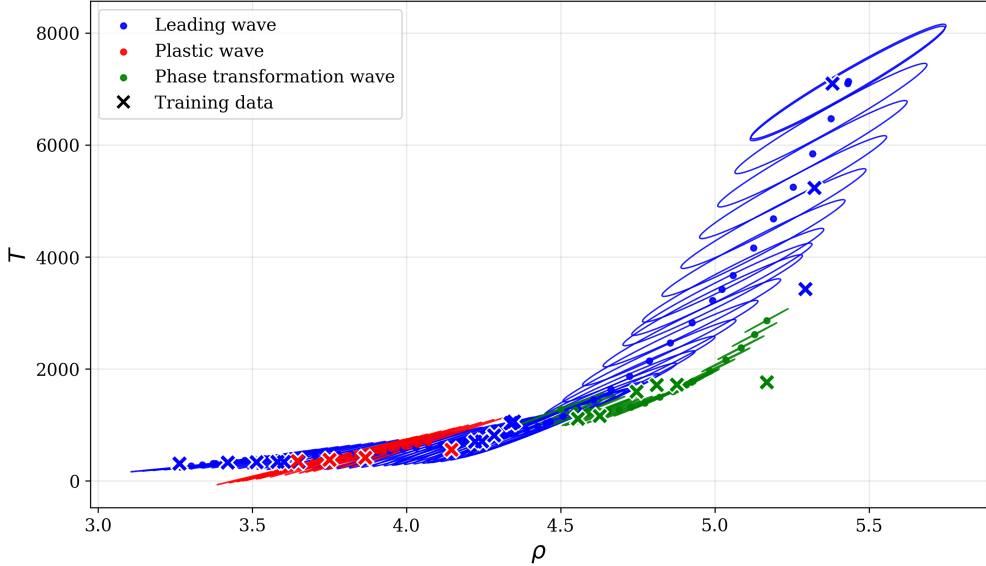


Figure 16: Predicted temperature-density Hugoniot states based on the proposed GP model. The circular markers denote the mean predictions and the ellipses represent ± 2 std constant-probability covariance contours. The crosses indicate the training data used for each wave regime.

6. Concluding remarks

Progress in shock physics has long relied on experimentation and modeling. Plate-impact and laser-driven experiments are standard tools for characterizing shock behavior and enabling insights into extreme phenomena that are far removed from quasi-static loading. Such experiments are, however, constrained by technical limitations related to the observation of extremely fast scales. Molecular dynamics simulations have extended this frontier by uncovering atomistic mechanisms of deformation and transformation, but their substantial computational demands restrict their broader use. To overcome these challenges, the present work introduces a physics-constrained Gaussian Process (GP) regression framework that embeds the Rankine–Hugoniot jump conditions directly into the covariance structure. Relying on relatively small number of MD data, the framework yields thermodynamically consistent Hugoniot states and captures the transitions across elastic, plastic, and overdriven regimes with quantifiable uncertainty.

The proposed approach aligns with the broader goal of autonomous and data-driven materials discovery under extreme conditions. By embedding thermodynamics laws into the proposed probabilistic surrogate in conjunction with active learning strategies, it becomes possible to establish a closed-loop process in which simulations and experiments are chosen strategically to maximize information gain. Such an approach echoes recent advances in autonomous experimentation, where Gaussian Processes have been used to navigate high-dimensional parameter spaces while accounting for inhomogeneous noise. Extending these concepts to MD simulations in shock physics can potentially drastically reduce costly trial-and-error efforts in materials discovery.

7. Declaration of Competing Interest

The authors declare no competing interests.

8. Acknowledgements

Research was sponsored by the Army Research Laboratory and was accomplished under Cooperative Agreement Number W911NF-22-2-0121. The views and conclusions contained in this document are those of the authors and should not be interpreted as representing the official policies, either expressed or implied, of the Army Research Laboratory or the U.S. Government. The U.S. Government is authorized to reproduce and distribute reprints for Government purposes notwithstanding any copyright notation herein.

Appendix A. Covariance derivation for the block covariance model

Covariance derivation for the block covariance model in Eq. (32)

$$\begin{aligned}\text{Cov}(y_l^j, y_m^k) &= \mathbb{E}\left[\left(y_l^j - \mathbb{E}[y_l^j]\right)\left(y_m^k - \mathbb{E}[y_m^k]\right)\right] \\ &= \mathbb{E}[y_l^j y_m^k] - \mathbb{E}[y_l^j] \mathbb{E}[y_m^k]\end{aligned}\quad (\text{A.1})$$

We define:

$$\begin{aligned}\mathbf{I}_1 &= \mathbb{E}[y_l^j y_m^k] \\ \mathbf{I}_2 &= \mathbb{E}[y_l^j] \mathbb{E}[y_m^k]\end{aligned}\quad (\text{A.2})$$

Grouping the terms:

Zeroth-order term

$$A_l^j = f_l(\bar{x}_j) \quad (\text{A.3})$$

First-order term

$$B_l^j = \frac{\partial f_l}{\partial u_{s_i}} \bigg|_{\bar{x}_j} (u_{s_i}^j - \bar{u}_{s_i}^j) + \frac{\partial f_l}{\partial \nu_{z_i}} \bigg|_{\bar{x}_j} (\nu_{z_i}^j - \bar{\nu}_{z_i}^j) \quad (\text{A.4})$$

Second-order term

$$\begin{aligned}C_l^j &= \frac{1}{2} \frac{\partial^2 f_l}{\partial (u_{s_i})^2} \bigg|_{\bar{x}_j} (u_{s_i}^j - \bar{u}_{s_i}^j)^2 + \frac{1}{2} \frac{\partial^2 f_l}{\partial (\nu_{z_i})^2} \bigg|_{\bar{x}_j} (\nu_{z_i}^j - \bar{\nu}_{z_i}^j)^2 \\ &+ \frac{\partial^2 f_l}{\partial u_{s_i} \partial \nu_{z_i}} \bigg|_{\bar{x}_j} (u_{s_i}^j - \bar{u}_{s_i}^j)(\nu_{z_i}^j - \bar{\nu}_{z_i}^j)\end{aligned}\quad (\text{A.5})$$

Similarly,

$$y_m^k = A_m^k + B_m^k + C_m^k + \dots \quad (\text{A.6})$$

Multiplying out and neglecting higher-order interactions:

$$\begin{aligned}y_l^j y_m^k &= A_l^j A_m^k + A_l^j B_m^k + A_l^j C_m^k \\ &+ B_l^j A_m^k + B_l^j B_m^k + B_l^j C_m^k \\ &+ C_l^j A_m^k + C_l^j B_m^k + C_l^j C_m^k + \dots\end{aligned}\quad (\text{A.7})$$

Taking expectations, using $\mathbb{E}[B_l^j] = 0$, we get:

$$\mathbf{I}_1 = A_l^j A_m^k + A_l^j \mathbb{E}[C_m^k] + \mathbb{E}[B_l^j B_m^k] + \mathbb{E}[C_l^j] A_m^k \quad (\text{A.8})$$

$$\begin{aligned} \mathbf{I}_2 &= \mathbb{E}[y_l^j] \mathbb{E}[y_m^k] \\ &= A_l^j A_m^k + A_l^j \mathbb{E}[C_m^k] + \mathbb{E}[C_l^j] A_m^k + \mathbb{E}[C_l^j] \mathbb{E}[C_m^k] \end{aligned} \quad (\text{A.9})$$

Subtracting:

$$\text{Cov}(y_l^j, y_m^k) = \mathbb{E}[B_l^j B_m^k] - \mathbb{E}[C_l^j] \mathbb{E}[C_m^k] \quad (\text{A.10})$$

If we neglect the $\mathbb{E}[C_l^j] \mathbb{E}[C_m^k]$ term as higher-order, we obtain:

$$\begin{aligned} \text{Cov}(y_l^j, y_m^k) \approx \mathbb{E}[B_l^j B_m^k] &= \frac{\partial f_l}{\partial u_{s_i}} \Big|_{\bar{x}_j} \frac{\partial f_m}{\partial u_{s_i}} \Big|_{\bar{x}_k} \mathbf{K}_{u_{s_i} u_{s_i}}^{jk} \\ &+ \left(\frac{\partial f_l}{\partial u_{s_i}} \Big|_{\bar{x}_j} \frac{\partial f_m}{\partial \nu_{z_i}} \Big|_{\bar{x}_k} + \frac{\partial f_l}{\partial \nu_{z_i}} \Big|_{\bar{x}_j} \frac{\partial f_m}{\partial u_{s_i}} \Big|_{\bar{x}_k} \right) \cdot \mathbf{K}_{u_{s_i} \nu_{z_i}}^{jk} \\ &+ \frac{\partial f_l}{\partial \nu_{z_i}} \Big|_{\bar{x}_j} \frac{\partial f_m}{\partial \nu_{z_i}} \Big|_{\bar{x}_k} \mathbf{K}_{\nu_{z_i} \nu_{z_i}}^{jk} \end{aligned} \quad (\text{A.11})$$

Appendix B. Derivation of the Hugoniot-based derivatives

Considering the Hugoniot equations where indices i and j represent the material and the state, respectively. The Hugoniot equations are given as:

$$P_i^j = \rho_{i-1}^j (u_{s_i}^j - \nu_{z_{i-1}}^j) (\nu_{z_i}^j - \nu_{z_{i-1}}^j) + P_{i-1}^j \quad (\text{B.1})$$

$$\rho_i^j = \rho_{i-1}^j \frac{u_{s_i}^j - \nu_{z_{i-1}}^j}{u_{s_i}^j - \nu_{z_i}^j}. \quad (\text{B.2})$$

$$E_i^j = E_{i-1}^j + \frac{1}{2} (P_i^j + P_{i-1}^j) \left(\frac{1}{\rho_{i-1}^j} - \frac{1}{\rho_i^j} \right) \quad (\text{B.3})$$

Pressure Derivatives.

$$\frac{\partial P_i^j}{\partial u_{s_i}^j} = \rho_{i-1}^j (\nu_{z_i}^j - \nu_{z_{i-1}}^j) \quad (\text{B.4})$$

$$\frac{\partial P_i^j}{\partial \nu_{z_i}^j} = \rho_{i-1}^j (u_{s_i}^j - \nu_{z_{i-1}}^j) \quad (\text{B.5})$$

$$\frac{\partial^2 P_i^j}{\partial (u_{s_i}^j)^2} = 0 \quad (\text{B.6})$$

$$\frac{\partial^2 P_i^j}{\partial (\nu_{z_i}^j)^2} = 0 \quad (\text{B.7})$$

$$\frac{\partial^2 P_i^j}{\partial u_{s_i}^j \partial \nu_{z_i}^j} = \rho_{i-1}^j \quad (\text{B.8})$$

Density Derivatives.

$$\frac{\partial \rho_i^j}{\partial u_{s_i}^j} = \rho_{i-1}^j \frac{\nu_{z_i}^j - \nu_{z_{i-1}}^j}{(u_{s_i}^j - \nu_{z_i}^j)^2} \quad (\text{B.9})$$

$$\frac{\partial \rho_i^j}{\partial \nu_{z_i}^j} = \rho_{i-1}^j \frac{u_{s_i}^j - \nu_{z_{i-1}}^j}{(u_{s_i}^j - \nu_{z_i}^j)^2} \quad (\text{B.10})$$

$$\frac{\partial^2 \rho_i^j}{\partial (u_{s_i}^j)^2} = 2\rho_{i-1}^j \frac{\nu_{z_{i-1}}^j - \nu_{z_i}^j}{(u_{s_i}^j - \nu_{z_i}^j)^3} \quad (\text{B.11})$$

$$\frac{\partial^2 \rho_i^j}{\partial (\nu_{z_i}^j)^2} = 2\rho_{i-1}^j \frac{u_{s_i}^j - \nu_{z_{i-1}}^j}{(u_{s_i}^j - \nu_{z_i}^j)^3} \quad (\text{B.12})$$

$$\frac{\partial^2 \rho_i^j}{\partial u_{s_i}^j \partial \nu_{z_i}^j} = -2\rho_{i-1}^j \frac{u_{s_i}^j - \nu_{z_{i-1}}^j}{(u_{s_i}^j - \nu_{z_i}^j)^3} \quad (\text{B.13})$$

Energy Definition.

$$E_i^j = E_{i-1}^j + \frac{1}{2}(\nu_{z_i}^j - \nu_{z_{i-1}}^j)^2 + P_{i-1}^j \cdot \frac{1}{\rho_{i-1}^j} \frac{\nu_{z_i}^j - \nu_{z_{i-1}}^j}{u_{s_i}^j - \nu_{z_{i-1}}^j} \quad (\text{B.14})$$

Energy Derivatives.

$$\frac{\partial E_i^j}{\partial u_{s_i}^j} = -\frac{P_{i-1}^j}{\rho_{i-1}^j} \frac{\nu_{z_i}^j - \nu_{z_{i-1}}^j}{(u_{s_i}^j - \nu_{z_{i-1}}^j)^2} \quad (\text{B.15})$$

$$\frac{\partial E_i^j}{\partial \nu_{z_i}^j} = (\nu_{z_i}^j - \nu_{z_{i-1}}^j) + \frac{P_{i-1}^j}{\rho_{i-1}^j (u_{s_i}^j - \nu_{z_{i-1}}^j)} \quad (\text{B.16})$$

$$\frac{\partial^2 E_i^j}{\partial (u_{s_i}^j)^2} = 2\frac{P_{i-1}^j}{\rho_{i-1}^j} \frac{\nu_{z_i}^j - \nu_{z_{i-1}}^j}{(u_{s_i}^j - \nu_{z_{i-1}}^j)^3} \quad (\text{B.17})$$

$$\frac{\partial^2 E_i^j}{\partial (\nu_{z_i}^j)^2} = 1 \quad (\text{B.18})$$

$$\frac{\partial^2 E_i^j}{\partial u_{s_i}^j \partial \nu_{z_i}^j} = -\frac{P_{i-1}^j}{\rho_{i-1}^j} \frac{1}{(u_{s_i}^j - \nu_{z_{i-1}}^j)^2} \quad (\text{B.19})$$

Temperature derivatives

$$T_i^j = a + bE_i^j \quad (\text{B.20})$$

$$\frac{\partial T_i^j}{\partial u_{s_i}^j} = b \frac{\partial E_i^j}{\partial u_{s_i}^j} \quad (\text{B.21})$$

$$\frac{\partial T_i^j}{\partial \nu_{z_i}^j} = b \frac{\partial E_i^j}{\partial \nu_{z_i}^j} \quad (\text{B.22})$$

$$\frac{\partial^2 T_i^j}{\partial (u_{s_i}^j)^2} = b \frac{\partial^2 E_i^j}{\partial (u_{s_i}^j)^2} \quad (\text{B.23})$$

$$\frac{\partial^2 T_i^j}{\partial (\nu_{z_i}^j)^2} = b \frac{\partial^2 E_i^j}{\partial (\nu_{z_i}^j)^2} \quad (\text{B.24})$$

$$\frac{\partial^2 T_i^j}{\partial u_{s_i}^j \partial \nu_{z_i}^j} = b \frac{\partial^2 E_i^j}{\partial u_{s_i}^j \partial \nu_{z_i}^j} \quad (\text{B.25})$$

Appendix C. Mean and covariances for Thermodynamic State Variables

Consider the Taylor expansion mean and covariance expressions in Eqs. (35) and (36), respectively. Using the analytical derivatives in [Appendix B](#), the explicit expression of the thermodynamic variables are given below. The index i denotes the propagating wave front, and j and k are the data points of the l^{th} and m^{th} output variables.

$$P_i^j = \rho_{i-1}^j (u_{s_i}^j - \nu_{z_{i-1}}^j) (\nu_{z_i}^j - \nu_{z_{i-1}}^j) + P_{i-1}^j \quad (\text{C.1})$$

Mean pressure

Using Eq. (B.1)

$$\bar{P}_i^j = \rho_{i-1}^j (\bar{u}_{s_i}^j - \nu_{z_{i-1}}^j) (\bar{\nu}_{z_i}^j - \nu_{z_{i-1}}^j) + P_{i-1}^j + \rho_{i-1}^j \mathbf{K}_{u_{s_i} \nu_{z_i}}^{jj} \quad (\text{C.2})$$

Pressure covariances

Using the derivatives in Eqs. (B.4)-(B.8) yields

$$\begin{aligned} \mathbf{K}_{P_i P_i}^{jk} &= \rho_{i-1}^j (\bar{\nu}_{z_i}^j - \nu_{z_{i-1}}^j) \rho_{i-1}^k (\bar{\nu}_{z_i}^k - \nu_{z_{i-1}}^k) \mathbf{K}_{u_{s_i} u_{s_i}}^{jk} \\ &+ \left[\rho_{i-1}^j (\bar{\nu}_{z_i}^j - \nu_{z_{i-1}}^j) \rho_{i-1}^k (\bar{u}_{s_i}^k - \nu_{z_{i-1}}^k) + \rho_{i-1}^j (\bar{u}_{s_i}^j - \nu_{z_{i-1}}^j) \rho_{i-1}^k (\bar{\nu}_{z_i}^k - \nu_{z_{i-1}}^k) \right] \mathbf{K}_{u_{s_i} \nu_{z_i}}^{jk} \\ &+ \rho_{i-1}^j (\bar{u}_{s_i}^j - \nu_{z_{i-1}}^j) \rho_{i-1}^k (\bar{u}_{s_i}^k - \nu_{z_{i-1}}^k) \mathbf{K}_{\nu_{z_i} \nu_{z_i}}^{jk} \end{aligned} \quad (\text{C.3})$$

Mean density

Using Eq. (B.2) gives

$$\begin{aligned} \bar{\rho}_i^j &= \rho_{i-1}^j \frac{\bar{u}_{s_i}^j - \nu_{z_{i-1}}^j}{\bar{u}_{s_i}^j - \bar{\nu}_{z_i}^j} \\ &+ \rho_{i-1}^j \frac{(\nu_{z_{i-1}}^j - \bar{\nu}_{z_i}^j) \mathbf{K}_{u_{s_i} u_{s_i}}^{jj} + (\bar{u}_{s_i}^j - \nu_{z_{i-1}}^j) \mathbf{K}_{\nu_{z_i} \nu_{z_i}}^{jj} - 2(\bar{u}_{s_i}^j - \nu_{z_{i-1}}^j) \mathbf{K}_{u_{s_i} \nu_{z_i}}^{jj}}{(\bar{u}_{s_i}^j - \bar{\nu}_{z_i}^j)^3} \end{aligned} \quad (\text{C.4})$$

Density covariances

Using the derivatives in Eqs. (B.9)-(B.13) yields

$$\begin{aligned}
\mathbf{K}_{\rho_i \rho_i}^{jk} &= \frac{\rho_{i-1}^j (\bar{\nu}_{z_i}^j - \nu_{z_{i-1}}^j) \rho_{i-1}^k (\bar{\nu}_{z_i}^k - \nu_{z_{i-1}}^k)}{(\bar{u}_{s_i}^j - \bar{\nu}_{z_i}^j)^2} \mathbf{K}_{u_{s_i} u_{s_i}}^{jk} \\
&+ \left[\frac{\rho_{i-1}^j (\bar{\nu}_{z_i}^j - \nu_{z_{i-1}}^j) \rho_{i-1}^k (\bar{u}_{s_i}^k - \nu_{z_{i-1}}^k)}{(\bar{u}_{s_i}^j - \bar{\nu}_{z_i}^j)^2} \right. \\
&\quad \left. + \frac{\rho_{i-1}^j (\bar{u}_{s_i}^j - \nu_{z_{i-1}}^j) \rho_{i-1}^k (\bar{\nu}_{z_i}^k - \nu_{z_{i-1}}^k)}{(\bar{u}_{s_i}^j - \bar{\nu}_{z_i}^j)^2} \right] \mathbf{K}_{u_{s_i} \nu_{z_i}}^{jk} \\
&+ \frac{\rho_{i-1}^j (\bar{u}_{s_i}^j - \nu_{z_{i-1}}^j) \rho_{i-1}^k (\bar{u}_{s_i}^k - \nu_{z_{i-1}}^k)}{(\bar{u}_{s_i}^j - \bar{\nu}_{z_i}^j)^2} \mathbf{K}_{\nu_{z_i} \nu_{z_i}}^{jk}
\end{aligned} \tag{C.5}$$

Mean energy

Using Eqs. (B.1)-(B.3) gives

$$\begin{aligned}
\bar{E}_i^j &= E_{i-1}^j + \frac{1}{2} (\bar{\nu}_{z_i}^j - \nu_{z_{i-1}}^j)^2 + \frac{P_{i-1}^j}{\rho_{i-1}^j} \frac{\bar{\nu}_{z_i}^j - \nu_{z_{i-1}}^j}{\bar{u}_{s_i}^j - \nu_{z_{i-1}}^j} \\
&+ \frac{1}{2} \left[\left(2 \frac{P_{i-1}^j}{\rho_{i-1}^j} \frac{\bar{\nu}_{z_i}^j - \nu_{z_{i-1}}^j}{(\bar{u}_{s_i}^j - \nu_{z_{i-1}}^j)^3} \right) \mathbf{K}_{u_{s_i} u_{s_i}}^{jj} + \mathbf{K}_{\nu_{z_i} \nu_{z_i}}^{jj} \right. \\
&\quad \left. - 2 \frac{P_{i-1}^j}{\rho_{i-1}^j} \frac{1}{(\bar{u}_{s_i}^j - \nu_{z_{i-1}}^j)^2} \mathbf{K}_{u_{s_i} \nu_{z_i}}^{jj} \right]
\end{aligned} \tag{C.6}$$

Energy covariances

Using the derivatives in Eqs. (B.15)-(B.19) yields

$$\begin{aligned}
\mathbf{K}_{E_i E_i}^{jk} &= \left(- \frac{P_{i-1}^j}{\rho_{i-1}^j} \frac{\bar{\nu}_{z_i}^j - \nu_{z_{i-1}}^j}{(\bar{u}_{s_i}^j - \nu_{z_{i-1}}^j)^2} \right) \left(- \frac{P_{i-1}^k}{\rho_{i-1}^k} \frac{\bar{\nu}_{z_i}^k - \nu_{z_{i-1}}^k}{(\bar{u}_{s_i}^k - \nu_{z_{i-1}}^k)^2} \right) \mathbf{K}_{u_{s_i} u_{s_i}}^{jk} \\
&+ \left[- \frac{P_{i-1}^j}{\rho_{i-1}^j} \frac{\bar{\nu}_{z_i}^j - \nu_{z_{i-1}}^j}{(\bar{u}_{s_i}^j - \nu_{z_{i-1}}^j)^2} \left(\bar{\nu}_{z_i}^k - \nu_{z_{i-1}}^k + \frac{P_{i-1}^k}{\rho_{i-1}^k} \frac{1}{\bar{u}_{s_i}^k - \nu_{z_{i-1}}^k} \right) \right. \\
&\quad \left. + \left(\bar{\nu}_{z_i}^j - \nu_{z_{i-1}}^j + \frac{P_{i-1}^j}{\rho_{i-1}^j} \frac{1}{\bar{u}_{s_i}^j - \nu_{z_{i-1}}^j} \right) \left(- \frac{P_{i-1}^k}{\rho_{i-1}^k} \frac{\bar{\nu}_{z_i}^k - \nu_{z_{i-1}}^k}{(\bar{u}_{s_i}^k - \nu_{z_{i-1}}^k)^2} \right) \right] \mathbf{K}_{u_{s_i} \nu_{z_i}}^{jk} \\
&+ \left(\bar{\nu}_{z_i}^j - \nu_{z_{i-1}}^j + \frac{P_{i-1}^j}{\rho_{i-1}^j} \frac{1}{\bar{u}_{s_i}^j - \nu_{z_{i-1}}^j} \right) \left(\bar{\nu}_{z_i}^k - \nu_{z_{i-1}}^k + \frac{P_{i-1}^k}{\rho_{i-1}^k} \frac{1}{\bar{u}_{s_i}^k - \nu_{z_{i-1}}^k} \right) \mathbf{K}_{\nu_{z_i} \nu_{z_i}}^{jk}
\end{aligned} \tag{C.7}$$

Pressure-shock velocity cross-covariance

Using the derivatives in Eqs. (B.4)-(B.8) one obtains

$$\mathbf{K}_{P_i u_{s_i}}^{jk} = \rho_{i-1}^j (\bar{\nu}_{z_i}^j - \nu_{z_{i-1}}^j) \mathbf{K}_{u_{s_i} u_{s_i}}^{jk} + \rho_{i-1}^j (\bar{u}_{s_i}^j - \nu_{z_{i-1}}^j) \mathbf{K}_{u_{s_i} \nu_{z_i}}^{jk} \tag{C.8}$$

Pressure-particle velocity cross-covariance

Using the derivatives in Eqs. (B.4)–(B.8) leads to

$$\mathbf{K}_{P_i \nu_{z_i}}^{jk} = \rho_{i-1}^j (\bar{\nu}_{z_i}^j - \nu_{z_{i-1}}^j) \mathbf{K}_{u_{s_i} \nu_{z_i}}^{jk} + \rho_{i-1}^j (\bar{u}_{s_i}^j - \nu_{z_{i-1}}^j) \mathbf{K}_{\nu_{z_i} \nu_{z_i}}^{jk} \quad (\text{C.9})$$

Pressure-density cross covariance

Using Eqs. (B.4)–(B.8) and (B.9)–(B.13) yields

$$\begin{aligned} \mathbf{K}_{P_i \rho_i}^{jk} &= \rho_{i-1}^j (\bar{\nu}_{z_i}^j - \nu_{z_{i-1}}^j) \frac{\rho_{i-1}^k (\bar{\nu}_{z_i}^k - \nu_{z_{i-1}}^k)}{(\bar{u}_{s_i}^k - \bar{\nu}_{z_i}^k)^2} \mathbf{K}_{u_{s_i} u_{s_i}}^{jk} \\ &+ \left[\rho_{i-1}^j (\bar{\nu}_{z_i}^j - \nu_{z_{i-1}}^j) \frac{\rho_{i-1}^k (\bar{u}_{s_i}^k - \nu_{z_{i-1}}^k)}{(\bar{u}_{s_i}^k - \bar{\nu}_{z_i}^k)^2} + \rho_{i-1}^j (\bar{u}_{s_i}^j - \nu_{z_{i-1}}^j) \frac{\rho_{i-1}^k (\bar{\nu}_{z_i}^k - \nu_{z_{i-1}}^k)}{(\bar{u}_{s_i}^k - \bar{\nu}_{z_i}^k)^2} \right] \mathbf{K}_{u_{s_i} \nu_{z_i}}^{jk} \\ &+ \rho_{i-1}^j (\bar{u}_{s_i}^j - \nu_{z_{i-1}}^j) \frac{\rho_{i-1}^k (\bar{u}_{s_i}^k - \nu_{z_{i-1}}^k)}{(\bar{u}_{s_i}^k - \bar{\nu}_{z_i}^k)^2} \mathbf{K}_{\nu_{z_i} \nu_{z_i}}^{jk} \end{aligned} \quad (\text{C.10})$$

Pressure-energy cross-covariance

Using the derivatives in Eqs. (B.4)–(B.8) and (B.15)–(B.19) one obtains

$$\begin{aligned} \mathbf{K}_{P_i E_i}^{jk} &= \rho_{i-1}^j (\bar{\nu}_{z_i}^j - \nu_{z_{i-1}}^j) \left[-\frac{P_{i-1}^k - \bar{\nu}_{z_i}^k - \nu_{z_{i-1}}^k}{\rho_{i-1}^k (\bar{u}_{s_i}^k - \nu_{z_{i-1}}^k)^2} \right] \mathbf{K}_{u_{s_i} u_{s_i}}^{jk} \\ &+ \left[\rho_{i-1}^j (\bar{\nu}_{z_i}^j - \nu_{z_{i-1}}^j) \left(\bar{\nu}_{z_i}^k - \nu_{z_{i-1}}^k + \frac{P_{i-1}^k}{\rho_{i-1}^k} \frac{1}{\bar{u}_{s_i}^k - \nu_{z_{i-1}}^k} \right) \right. \\ &\quad \left. + \rho_{i-1}^j (\bar{u}_{s_i}^j - \nu_{z_{i-1}}^j) \left[-\frac{P_{i-1}^k - \bar{\nu}_{z_i}^k - \nu_{z_{i-1}}^k}{\rho_{i-1}^k (\bar{u}_{s_i}^k - \nu_{z_{i-1}}^k)^2} \right] \right] \mathbf{K}_{u_{s_i} \nu_{z_i}}^{jk} \\ &+ \rho_{i-1}^j (\bar{u}_{s_i}^j - \nu_{z_{i-1}}^j) \left(\bar{\nu}_{z_i}^k - \nu_{z_{i-1}}^k + \frac{P_{i-1}^k}{\rho_{i-1}^k} \frac{1}{\bar{u}_{s_i}^k - \nu_{z_{i-1}}^k} \right) \mathbf{K}_{\nu_{z_i} \nu_{z_i}}^{jk} \end{aligned} \quad (\text{C.11})$$

Density-shock velocity cross-covariance

Using the derivatives in Eqs. (B.9)–(B.13) one obtains

$$\mathbf{K}_{\rho_i u_{s_i}}^{jk} = \frac{\rho_{i-1}^j (\bar{\nu}_{z_i}^j - \nu_{z_{i-1}}^j)}{(\bar{u}_{s_i}^j - \bar{\nu}_{z_i}^j)^2} \mathbf{K}_{u_{s_i} u_{s_i}}^{jk} + \frac{\rho_{i-1}^j (\bar{u}_{s_i}^j - \nu_{z_{i-1}}^j)}{(\bar{u}_{s_i}^j - \bar{\nu}_{z_i}^j)^2} \mathbf{K}_{u_{s_i} \nu_{z_i}}^{jk} \quad (\text{C.12})$$

Density-particle velocity cross-covariance

Using the same derivatives gives

$$\mathbf{K}_{\rho_i \nu_{z_i}}^{jk} = \frac{\rho_{i-1}^j (\bar{\nu}_{z_i}^j - \nu_{z_{i-1}}^j)}{(\bar{u}_{s_i}^j - \bar{\nu}_{z_i}^j)^2} \mathbf{K}_{u_{s_i} \nu_{z_i}}^{jk} + \frac{\rho_{i-1}^j (\bar{u}_{s_i}^j - \nu_{z_{i-1}}^j)}{(\bar{u}_{s_i}^j - \bar{\nu}_{z_i}^j)^2} \mathbf{K}_{\nu_{z_i} \nu_{z_i}}^{jk} \quad (\text{C.13})$$

Density-energy cross-covariance

Using the derivatives in Eqs. (B.9)–(B.13) and (B.15)–(B.19) one obtains

$$\begin{aligned}
\mathbf{K}_{\rho_i E_i}^{jk} = & \frac{\rho_{i-1}^j (\bar{\nu}_{z_i}^j - \nu_{z_{i-1}}^j)}{(\bar{u}_{s_i}^j - \bar{\nu}_{z_i}^j)^2} \left[-\frac{P_{i-1}^k}{\rho_{i-1}^k} \frac{\bar{\nu}_{z_i}^k - \nu_{z_{i-1}}^k}{(\bar{u}_{s_i}^k - \nu_{z_{i-1}}^k)^2} \right] \mathbf{K}_{u_{s_i} u_{s_i}}^{jk} \\
& + \left[\frac{\rho_{i-1}^j (\bar{\nu}_{z_i}^j - \nu_{z_{i-1}}^j)}{(\bar{u}_{s_i}^j - \bar{\nu}_{z_i}^j)^2} \left(\bar{\nu}_{z_i}^k - \nu_{z_{i-1}}^k + \frac{P_{i-1}^k}{\rho_{i-1}^k} \frac{1}{\bar{u}_{s_i}^k - \nu_{z_{i-1}}^k} \right) \right. \\
& \quad \left. + \frac{\rho_{i-1}^j (\bar{u}_{s_i}^j - \nu_{z_{i-1}}^j)}{(\bar{u}_{s_i}^j - \bar{\nu}_{z_i}^j)^2} \left[-\frac{P_{i-1}^k}{\rho_{i-1}^k} \frac{\bar{\nu}_{z_i}^k - \nu_{z_{i-1}}^k}{(\bar{u}_{s_i}^k - \nu_{z_{i-1}}^k)^2} \right] \right] \mathbf{K}_{u_{s_i} \nu_{z_i}}^{jk} \\
& + \frac{\rho_{i-1}^j (\bar{u}_{s_i}^j - \nu_{z_{i-1}}^j)}{(\bar{u}_{s_i}^j - \bar{\nu}_{z_i}^j)^2} \left(\bar{\nu}_{z_i}^k - \nu_{z_{i-1}}^k + \frac{P_{i-1}^k}{\rho_{i-1}^k} \frac{1}{\bar{u}_{s_i}^k - \nu_{z_{i-1}}^k} \right) \mathbf{K}_{\nu_{z_i} \nu_{z_i}}^{jk}
\end{aligned} \tag{C.14}$$

Energy-shock velocity cross-covariance

Using the derivatives in Eqs. (B.15)–(B.19) one obtains

$$\begin{aligned}
\mathbf{K}_{E_i u_{s_i}}^{jk} = & \left[-\frac{P_{i-1}^j}{\rho_{i-1}^j} \frac{\bar{\nu}_{z_i}^j - \nu_{z_{i-1}}^j}{(\bar{u}_{s_i}^j - \nu_{z_{i-1}}^j)^2} \right] \mathbf{K}_{u_{s_i} u_{s_i}}^{jk} \\
& + \left[\bar{\nu}_{z_i}^j - \nu_{z_{i-1}}^j + \frac{P_{i-1}^j}{\rho_{i-1}^j} \frac{1}{\bar{u}_{s_i}^j - \nu_{z_{i-1}}^j} \right] \mathbf{K}_{\nu_{z_i} u_{s_i}}^{jk}
\end{aligned} \tag{C.15}$$

Energy-particle velocity cross-covariance

Using the same derivatives gives

$$\begin{aligned}
\mathbf{K}_{E_i \nu_{z_i}}^{jk} = & \left[-\frac{P_{i-1}^j}{\rho_{i-1}^j} \frac{\bar{\nu}_{z_i}^j - \nu_{z_{i-1}}^j}{(\bar{u}_{s_i}^j - \nu_{z_{i-1}}^j)^2} \right] \mathbf{K}_{u_{s_i} \nu_{z_i}}^{jk} \\
& + \left[\bar{\nu}_{z_i}^j - \nu_{z_{i-1}}^j + \frac{P_{i-1}^j}{\rho_{i-1}^j} \frac{1}{\bar{u}_{s_i}^j - \nu_{z_{i-1}}^j} \right] \mathbf{K}_{\nu_{z_i} \nu_{z_i}}^{jk}
\end{aligned} \tag{C.16}$$

References

- [1] T. Vogler, W. Reinhart, L. Chhabildas, D. Dandekar, Hugoniot and strength behavior of silicon carbide, *Journal of Applied Physics* 99 (2) (2006).
- [2] B. W. Hamilton, M. N. Sakano, C. Li, A. Strachan, Chemistry under shock conditions, *Annual Review of Materials Research* 51 (1) (2021) 101–130.
- [3] B. L. Holian, P. S. Lomdahl, Plasticity induced by shock waves in nonequilibrium molecular-dynamics simulations, *Science* 280 (5372) (1998) 2085–2088.
- [4] K. Kadau, T. C. Germann, P. S. Lomdahl, B. L. Holian, Microscopic view of structural phase transitions induced by shock waves, *science* 296 (5573) (2002) 1681–1684.

- [5] A. Strachan, T. Çağın, W. A. Goddard III, Critical behavior in spallation failure of metals, *Physical Review B* 63 (6) (2001) 060103.
- [6] D. Thürmer, S. Zhao, O. R. Deluigi, C. Stan, I. A. Alhafez, H. M. Urbassek, M. A. Meyers, E. M. Bringa, N. Gunkelmann, Exceptionally high spallation strength for a high-entropy alloy demonstrated by experiments and simulations, *Journal of Alloys and Compounds* 895 (2022) 162567.
- [7] M. J. Cherukara, T. P. Weihs, A. Strachan, Molecular dynamics simulations of the reaction mechanism in ni/al reactive intermetallics, *Acta Materialia* 96 (2015) 1–9.
- [8] M. A. Wood, D. E. Kittell, C. D. Yarrington, A. P. Thompson, Multiscale modeling of shock wave localization in porous energetic material, *Physical Review B* 97 (1) (2018) 014109.
- [9] K. Kadau, T. C. Germann, P. S. Lomdahl, R. C. Albers, J. S. Wark, A. Higginbotham, B. L. Holian, Shock waves in polycrystalline iron, *Physical review letters* 98 (13) (2007) 135701.
- [10] J. Behler, Perspective: Machine learning potentials for atomistic simulations, *The Journal of chemical physics* 145 (17) (2016).
- [11] F. Noé, S. Olsson, J. Köhler, H. Wu, Boltzmann generators: Sampling equilibrium states of many-body systems with deep learning, *Science* 365 (6457) (2019) eaaw1147.
- [12] G. D. Pasparakis, L. Graham-Brady, M. D. Shields, Bayesian neural networks for predicting uncertainty in full-field material response, *Computer Methods in Applied Mechanics and Engineering* 433 (2025) 117486.
- [13] C. Li, J. C. Verduzco, B. H. Lee, R. J. Appleton, A. Strachan, Mapping microstructure to shock-induced temperature fields using deep learning, *npj Computational Materials* 9 (1) (2023) 178.
- [14] C. K. Williams, C. E. Rasmussen, Gaussian processes for machine learning, Vol. 2, MIT press Cambridge, MA, 2006.
- [15] J. A. Gaffney, L. Yang, S. Ali, Constraining model uncertainty in plasma equation-of-state models with a physics-constrained gaussian process, *arXiv preprint arXiv:2207.00668* (2022).
- [16] H. Sharma, J. A. Gaffney, D. Tsapetis, M. D. Shields, Learning thermodynamically constrained equations of state with uncertainty, *APL Machine Learning* 2 (1) (2024).
- [17] J. R. Asay, M. Shahinpoor, High-pressure shock compression of solids, Springer Science & Business Media, 2012.
- [18] A. P. Thompson, H. M. Aktulga, R. Berger, D. S. Bolintineanu, W. M. Brown, P. S. Crozier, P. J. In't Veld, A. Kohlmeyer, S. G. Moore, T. D. Nguyen, et al., Lammps-a flexible simulation tool for particle-based materials modeling at the atomic, meso, and continuum scales, *Computer physics communications* 271 (2022) 108171.

[19] P. Vashishta, R. K. Kalia, A. Nakano, J. P. Rino, Interaction potential for silicon carbide: A molecular dynamics study of elastic constants and vibrational density of states for crystalline and amorphous silicon carbide, *Journal of applied physics* 101 (10) (2007).

[20] A. P. Thompson, S. J. Plimpton, W. Mattson, General formulation of pressure and stress tensor for arbitrary many-body interaction potentials under periodic boundary conditions, *The Journal of chemical physics* 131 (15) (2009).

[21] P. S. Branicio, D. J. Srolovitz, Local stress calculation in simulations of multicomponent systems, *Journal of Computational Physics* 228 (22) (2009) 8467–8479.

[22] P. S. Branicio, J. Zhang, J. P. Rino, A. Nakano, R. K. Kalia, P. Vashishta, Plane shock loading on mono-and nano-crystalline silicon carbide, *Applied Physics Letters* 112 (11) (2018).

[23] T. Vogler, W. Reinhart, L. Chhabildas, D. Dandekar, Hugoniot and strength behavior of silicon carbide, *Journal of Applied Physics* 99 (2) (2006).

[24] G. Stewart, M. Al-Khassaweneh, An implementation of the hdbscan* clustering algorithm, *Applied Sciences* 12 (5) (2022) 2405.

[25] F. Pedregosa, G. Varoquaux, A. Gramfort, V. Michel, B. Thirion, O. Grisel, M. Blondel, P. Prettenhofer, R. Weiss, V. Dubourg, et al., Scikit-learn: Machine learning in python, *the Journal of machine Learning research* 12 (2011) 2825–2830.

[26] M. Hunt, S. Clark, D. Mejia, S. Desai, A. Strachan, Sim2ls: Fair simulation workflows and data, *Plos one* 17 (3) (2022) e0264492.

[27] R. Desai, C. Li, A. Strachan, [Automated shock parsing from md trajectories](#) (Aug 2025).
`doi:doi:10.21981/T77B-SP41`.
 URL <https://nanohub.org/resources/shockparse>

[28] E. V. Bonilla, K. Chai, C. Williams, Multi-task gaussian process prediction, *Advances in neural information processing systems* 20 (2007).

[29] G. Casella, R. Berger, *Statistical inference*, CRC press, 2024.

[30] E. M. Constantinescu, M. Anitescu, Physics-based covariance models for gaussian processes with multiple outputs, *International Journal for Uncertainty Quantification* 3 (1) (2013).

[31] D. P. Bertsekas, Nonlinear programming, *Journal of the Operational Research Society* 48 (3) (1997) 334–334.

[32] R. H. Byrd, P. Lu, J. Nocedal, C. Zhu, A limited memory algorithm for bound constrained optimization, *SIAM Journal on scientific computing* 16 (5) (1995) 1190–1208.